# High Order Resolution in Reentry Flows in 3D

**Edisson Sávio de Góes Maciel[1*] and Cláudia Regina de Andrade[2]**

[1]*Aeronautical Engineering Division (IAE), Aeronautical Technological Institute (ITA), Rua Santa Clara, 245 – Cx. Postal 2029 – 12243-970, São José dos Campos, SP, Brazil.*
[2]*Aeronautical Engineering Division (IAE), Aeronautical Technological Institute (ITA), Praça Marechal do Ar Eduardo Gomes, 50 – 12228-900, São José dos Campos, SP, Brazil.*

***Authors' contributions***

*This work was carried out in collaboration between both authors. Author ESDGM designed the study, performed the statistical analysis, wrote the protocol, wrote the first draft of the manuscript, and managed the analyses of the study. Author CRDA managed the literature searches. Both authors read and approved the final manuscript.*

*Original Research Article*

## Abstract

This work focuses on a numerical simulation of reentry 3D-flows using high order resolution schemes. Euler and Navier-Stokes equations are studied, on conservative and finite volume approaches, and employing structured spatial discretization. The ENO (Essentially Non-Oscillatory) procedure is presented to a conserved variable interpolation process, using either the Newton method, to second-, third-, fourth- and fifth-orders of accuracy, or the Hermite method, to third- and fifth-orders of accuracy. Furthermore, the WENO (Weighted Essentially Non-Oscillatory) procedure is also tested, using the Newton interpolation process, to generate third- and fifth-orders of accuracy solutions. Results applying the MUSCL scheme (Monotone Upstream-centered Schemes for Conservation Laws) are also presented and serve as TVD (Total Variation Diminishing) benchmark purpose. In this context, the "hot gas" hypersonic thermochemical non-equilibrium 3D-flow around a blunt body has been simulated. The convergence process is accelerated to steady-state condition through a spatially variable time step procedure, which has proved effective gains in terms of computational acceleration. The reactive simulations involve Earth atmosphere chemical models of five and seven species, based on the Saxena and Nair and Blottner models, respectively. Results showed that the ENO procedure using Newton 5th-order interpolation scheme presents better overall solutions.

---

*\*Corresponding author: E-mail: edissonsavio@yahoo.com.br;*

## 1. Introduction

The study of hypersonic flows has gained momentum with the advent of concepts like the National AeroSpace Plane (NASP) and similar transatmospheric vehicles. Under the very high velocity and temperature conditions experienced by hypersonic vehicles, departure from chemical and thermal equilibrium occurs. Properties of air change dramatically as new chemical species are produced at the expense of others. The simple one temperature model used to describe the energy of air becomes inapplicable, and it becomes necessary to consider one or more additional temperatures (corresponding to vibrational and electronic energies). Determination of aerothermal loads on blunt bodies in such an environment is of great importance.

Analysis of non-equilibrium flow is rather complex because (1) the number of equations to be solved is much larger than the Navier-Stokes equations, and (2) there are additional terms like the species production, mass diffusion, and vibrational energy relaxation, etc., that appear in the governing equations. In a typical flight of the NASP flying at Mach 15, ionization is not expected to occur, and a 5-species air is adequate for the analysis (see [1]). Since the rotational characteristic temperatures for the constituent species (namely N, O, $N_2$, $O_2$ and NO) are small, the translational and rotational energy modes are assumed to be in equilibrium, whereas the vibrational energy mode is assumed to be in non-equilibrium.

The problems of chemical non-equilibrium in the shock layers over vehicles flying at high speeds and high altitudes in the Earth's atmosphere have been discussed by several investigators ([2-5]). Most of the existing computer codes for calculating the non-equilibrium reacting flow use the one-temperature model, which assumes that all of the internal energy modes of the gaseous species are in equilibrium with the translational mode ([4-5]). It has been pointed out that such a one-temperature description of the flow leads to a substantial overestimation of the rate of equilibrium because of the elevated vibrational temperature [3]. A three-temperature chemical-kinetic model has been proposed by [6] to describe the relaxation phenomena correctly in such a flight regime. However, the model is quite complex and requires many chemical rate parameters which are not yet known. As a compromise between the three-temperature and the conventional one-temperature model, a two-temperature chemical-kinetic model has been developed ([7-8]), which is designated herein as the TTv model. The TTv model uses one temperature T to characterize both the translational energy of the atoms and molecules and the rotational energy of the molecules, and another temperature Tv to characterize the vibrational energy of the molecules, translational energy of the electrons, and electronic excitation energy of atoms and molecules. The model has been applied to compute the thermodynamic properties behind a normal shock wave in a flow through a constant-area duct ([7-8]). Radiation emission from the non-equilibrium flow has been calculated using the Non-equilibrium Air Radiation (NEQAIR) program ([9-10]). The flow and the radiation computations have been packaged into a single computer program, the Shock-Tube Radiation Program (STRAP).

The development of high order accurate, non-oscillatory shock capturing schemes currently is an area of active interest ([11]). High order accuracy is important for more complicated unsteady inviscid problems and for direct simulation of compressible flows. It is fairly straightforward to incorporate high order accuracy in non-conservative finite difference methods, however, shock capturing will not be possible. Finite volume methods and conservative finite difference methods, which retain this property, are unfortunately limited to first or second order accuracy in most cases. An important reason for this limitation in accuracy is the use of Total Variation Diminishing (TVD) methods to obtain non-oscillatory solutions. TVD methods are limited to first order accuracy in more than one dimension close to shock regions, [12], and even in one dimension they reduce to first order accuracy at non-sonic local extrema ([13]).

Second order spatial accuracy can be achieved by introducing more upwind points or cells in the schemes. It has been noted that the projection stage, whereby the solution is projected in each cell face (i-1/2,j,k;

i+1/2,j,k) on piecewise constant states, is the cause of the first order space accuracy of the Godunov schemes ([14]). Hence, it is sufficient to modify the first projection stage without modifying the Riemann solver, in order to generate higher spatial approximations. The state variables at the interfaces are thereby obtained from an extrapolation between neighboring cell averages. This method for the generation of second order upwind schemes based on variable extrapolation is often referred to in the literature as the MUSCL ("Monotone Upstream-centered Schemes for Conservation Laws") approach. The use of nonlinear limiters in such procedure, with the intention of restricting the amplitude of the gradients appearing in the solution, avoiding thus the formation of new extrema, allows that first order upwind schemes be transformed in TVD high resolution schemes with the appropriate definition of such nonlinear limiters, assuring monotone preserving and total variation diminishing methods.

Several recent works [15-20] developed the so called Essentially Non-Oscillatory (ENO) schemes, which do not have such limitation and have uniform high order of accuracy outside discontinuities. The main feature of ENO schemes is that they use an adaptive stencil. At each grid cell or point a searching algorithm determines which part of the flow surrounding that grid cell or point is the smoothest. This stencil is then used to construct a high order accurate, conservative interpolation to determine the variables at the cell faces. This interpolation process can be applied to conservative variables, characteristic variables, or the fluxes, either defined as cell averaged or point values. The ENO scheme tries to minimize numerical oscillations around discontinuities by using predominantly data from the smooth parts of the flow field. Due to the constant stencil switching the ENO scheme is highly non-linear and only limited theoretical results are available ([15-16]).

Polynomial interpolation theory has a number of important uses ([21]). A special usage is in developing means for working with functions that are stored in tabular form. Methods like Lagrange, Newton, and Hermite are likely the most employed ones in this area. The Lagrange form of the interpolation polynomial can be used for interpolation to a function given in tabular form. A practical difficulty with Lagrange interpolation is that since the error term is difficult to apply, the degree of the polynomial needed for the desired accuracy is generally not known until the computations are determined ([22]). But there are other forms that are much more convenient. The Newton method uses the concept of divided differences to develop its polynomial approximation. It is much better for computation than the Lagrange formula. In other cases, it is convenient to consider polynomials p(x) that interpolate a function f(x), and in addition have the derivative polynomial p'(x) interpolating the derivative function f'(x). In such cases, the Hermite method is more advisable. Hermite interpolation determines a polynomial that agrees with the function and its derivative at specified points. Therefore, the ENO procedure herein employed is based on Newton and Hermite interpolation process.

The WENO (Weighted Essentially Non-Oscillatory) scheme of [23] is another way to overcome the drawbacks of ENO schemes while keeping the robustness and high order accuracy of these schemes. The idea is the following: instead of approximating the numerical flux using only one of the candidate stencils, one uses a convex combination of all the candidate stencils. Each of the candidate stencils is assigned a weight which determines the contribution of this stencil to the final approximation of the numerical flux. The weights can be defined in such a way that in smooth regions it approaches certain optimal values to achieve a higher order of accuracy [an kth-order ENO scheme leads to a (2k-1)th-order WENO scheme in the optical case], while in regions near discontinuities, the stencils which contain the discontinuities are assigned a nearly zero weight. Thus essentially non-oscillatory property is achieved by emulating ENO schemes around discontinuities and a higher order of accuracy is obtained by emulating upstream central schemes with the optimal weights away from the discontinuities ([24]). WENO schemes completely remove the logical statements, that appear in the ENO stencil choosing step. Another advantage of WENO schemes is that its flux is smoother than that of ENO schemes. This smoothness enables us to prove convergence of WENO schemes for smooth solutions using Strang's technique.

In this work, the Euler and Navier-Stokes equations, on conservative and finite volume contexts, employing structured spatial discretization, are studied. The ENO procedure is presented to a conserved variable interpolation process, using either the Newton method, to second-, third-, fourth- and fifth-orders of

accuracy, or the Hermite method, to third- and fifth-orders of accuracy. Moreover, the WENO procedure is presented, using the Newton interpolation process, to generate third- and fifth-orders of accuracy solutions. Results employing the MUSCL scheme are also obtained to provide a TVD benchmark solution. The numerical algorithms of [25-26] are used to perform the reentry flow numerical experiments, which give us an original contribution to the CFD community. The "hot gas" hypersonic 3D-flow around a blunt body is numerically simulated. The convergence process is accelerated to steady-state condition through a spatially variable time step procedure, which has proved effective gains in terms of computational acceleration (see [27-28]). The reactive simulations involve Earth atmosphere chemical models of five and seven species, based on the [29] and [30] models, respectively. Results have indicated that the ENO procedure using Newton 5th-order interpolation scheme presents better solutions in both qualitative and quantitative features.

The subsequent sections in this paper discuss (i) the 3D-Navier-Stokes mathematical formulation; (ii) MUSCL scheme; (iii) ENO scheme; (iv) Newton interpolation; (v) Hermite interpolation; (vi) WENO scheme; (vii) numerical algorithms; (viii) physical problem, meshes, and initial condition; (ix) results for inviscid as viscous cases; and finally (x) conclusions.

The paper suggests the comparison between MUSCL, ENO and WENO procedures to enhance high order resolution. The paper is original and innovative in the sense that these three procedures are used for the first time to compare re-entry flows in thermochemical non-equilibrium conditions using two upwind algorithms. Both algorithms are flux vector splitting ones, and their implementation in the current literature considers them only for a perfect gas condition and rarely for "hot gas" flow. The use of both schemes altogether applied to re-entry flows is also a significant contribution to the CFD literature. Moreover, the Hermite and the Newton interpolation methods were implemented together and compared. The treatment of MUSCL, ENO and WENO procedures in finite volumes and in three-dimensions is also a significant contribution of originality. In spite of the use of well know upwind schemes for perfect gas flows in the literature, its use in high order comparisons, reactive flows, and in three-dimensions is also an innovative contribution to the CFD community.

## 2. 3-D Navier-Stokes Equations

The reactive thermal and chemical non-equilibrium 3-D Navier-Stokes equations, and the Euler equations (obtained in the limit of high Reynolds number) were implemented on a finite volume approach. In this case, these equations in integral and conservative forms can be expressed by:

$$\frac{\partial}{\partial t}\int_V Q dV + \int_S \vec{F} \bullet \vec{n} dS = \int_V S_{CV} dV, \text{ with } \vec{F} = \left(E_e - E_v\right)\vec{i} + \left(F_e - F_v\right)\vec{j} + \left(G_e - G_v\right)\vec{k}, \quad (1)$$

where: Q is the vector of conserved variables, V is the volume of a computational cell, $\vec{F}$ is the complete flux vector, $\vec{n}$ is the unity vector normal to the flux face, S is the flux area, $S_{CV}$ is the chemical and vibrational source term, $E_e$, $F_e$ and $G_e$ are the convective flux vectors or the Euler flux vectors in the x, y and z directions, respectively, $E_v$, $F_v$ and $G_v$ are the viscous flux vectors in the x, y and z directions, respectively. The $\vec{i}$, $\vec{j}$ and $\vec{k}$ unity vectors define the Cartesian coordinate system. The present formulation is developed for the seven species chemical model, with the five species model being obtained by eliminating the equations for $NO^+$ and $e^-$. Hence, twelve (12) conservation equations are solved: one of general mass conservation, three of linear momentum conservation, one of total energy, six of species mass conservation and one of the vibrational internal energy of the molecules. Therefore, one of the species is absent of the iterative process. The CFD ("Computational Fluid Dynamics") literature recommends that the species of biggest mass fraction of the gaseous mixture should be omitted, aiming to result in a minor numerical accumulation error, corresponding to the biggest mixture constituent (in the case, the air). To the present study, in which is chosen a chemical model to the air composed of seven (7) chemical species (N, O, $N_2$, $O_2$,

NO, $NO^+$ and $e^-$) and eighteen (18) chemical reactions, being fifteen (15) dissociation reactions, two (2) of recombination, and one (1) of ionization, this species can be the $N_2$ or the $O_2$. It was chosen the $N_2$ for this work. The vectors Q, $E_e$, $F_e$, $G_e$, $E_v$, $F_v$, $G_v$ and $S_{CV}$ can be defined as follows ([31]):

$$Q = \left\{ \begin{array}{c} \rho \\ \rho u \\ \rho v \\ \rho w \\ e \\ \rho_1 \\ \rho_2 \\ \rho_4 \\ \rho_5 \\ \rho_6 \\ \rho_7 \\ \rho e_V \end{array} \right\}, \; E_e = \left\{ \begin{array}{c} \rho u \\ \rho u^2 + p \\ \rho uv \\ \rho uw \\ \rho Hu \\ \rho_1 u \\ \rho_2 u \\ \rho_4 u \\ \rho_5 u \\ \rho_6 u \\ \rho_7 u \\ \rho e_V u \end{array} \right\}, \; F_e = \left\{ \begin{array}{c} \rho v \\ \rho vu \\ \rho v^2 + p \\ \rho vw \\ \rho Hv \\ \rho_1 v \\ \rho_2 v \\ \rho_4 v \\ \rho_5 v \\ \rho_6 v \\ \rho_7 v \\ \rho e_V v \end{array} \right\}, \; G_e = \left\{ \begin{array}{c} \rho w \\ \rho wu \\ \rho wv \\ \rho w^2 + p \\ \rho Hw \\ \rho_1 w \\ \rho_2 w \\ \rho_4 w \\ \rho_5 w \\ \rho_6 w \\ \rho_7 w \\ \rho e_V w \end{array} \right\}; \tag{2}$$

$$E_v = \frac{1}{Re} \left\{ \begin{array}{c} 0 \\ \tau_{xx} \\ \tau_{xy} \\ \tau_{xz} \\ \tau_{xx}u + \tau_{xy}v + \tau_{xz}w - q_{f,x} - q_{v,x} - \phi_x \\ -\rho_1 v_{1x} \\ -\rho_2 v_{2x} \\ -\rho_4 v_{4x} \\ -\rho_5 v_{5x} \\ -\rho_6 v_{6x} \\ -\rho_7 v_{7x} \\ -q_{v,x} - \phi_{v,x} \end{array} \right\}, \; F_v = \frac{1}{Re} \left\{ \begin{array}{c} 0 \\ \tau_{xy} \\ \tau_{yy} \\ \tau_{yz} \\ \tau_{xy}u + \tau_{yy}v + \tau_{yz}w - q_{f,y} - q_{v,y} - \phi_y \\ -\rho_1 v_{1y} \\ -\rho_2 v_{2y} \\ -\rho_4 v_{4y} \\ -\rho_5 v_{5y} \\ -\rho_6 v_{6y} \\ -\rho_7 v_{7y} \\ -q_{v,y} - \phi_{v,y} \end{array} \right\}; \tag{3}$$

in which: $\rho$ is the mixture density; u, v and w are Cartesian components of the velocity vector in the x, y and z directions, respectively; p is the fluid static pressure; e is the fluid total energy; $\rho_1$, $\rho_2$, $\rho_4$, $\rho_5$, $\rho_6$, and $\rho_7$ are densities of the N, O, $O_2$, NO, $NO^+$, and $e^-$ respectively; H is the mixture total enthalpy; $e_V$ is the sum of the vibrational energy of the molecules; the $\tau$'s are the components of the viscous stress tensor; $q_{f,x}$, $q_{f,y}$ and $q_{f,z}$ are the frozen components of the Fourier-heat-flux vector in the x, y and z directions, respectively;

$$
G_v = \frac{1}{Re} \left\{ \begin{array}{c} 0 \\ \tau_{xz} \\ \tau_{yz} \\ \tau_{zz} \\ \tau_{xz}u + \tau_{yz}v + \tau_{zz}w - q_{f,z} - q_{v,z} - \phi_z \\ -\rho_1 v_{1z} \\ -\rho_2 v_{2z} \\ -\rho_4 v_{4z} \\ -\rho_5 v_{5z} \\ -\rho_6 v_{6z} \\ -\rho_7 v_{7z} \\ -q_{v,z} - \phi_{v,z} \end{array} \right\}, \quad S_{CV} = \left\{ \begin{array}{c} 0 \\ 0 \\ 0 \\ 0 \\ 0 \\ \dot{\omega}_1 \\ \dot{\omega}_2 \\ \dot{\omega}_4 \\ \dot{\omega}_5 \\ \dot{\omega}_6 \\ \dot{\omega}_7 \\ \sum_{s=mol} \rho_s \left(e^*_{v,s} - e_{v,s}\right)/\tau_s + \sum_{s=mol} \dot{\omega}_s e_{v,s} \end{array} \right\}; \quad (4)
$$

$q_{v,x}$, $q_{v,y}$ and $q_{v,z}$ are the components of the Fourier-heat-flux vector calculated with the vibrational thermal conductivity and vibrational temperature; $\rho_s v_{sx}$, $\rho_s v_{sy}$ and $\rho_s v_{sz}$ represent the species diffusion flux, defined by the Fick law; $\phi_x$, $\phi_y$ and $\phi_z$ are the terms of mixture diffusion; $\phi_{v,x}$, $\phi_{v,y}$ and $\phi_{v,z}$ are the terms of molecular diffusion calculated at the vibrational temperature; $\dot{\omega}_s$ is the chemical source term of each species equation, defined by the law of mass action; $e^*_v$ is the molecular-vibrational-internal energy calculated with the translational/rotational temperature; and $\tau_s$ is the translational-vibrational characteristic relaxation time of each molecule.

The viscous stresses, in N/m$^2$, are determined, according to a Newtonian fluid model, by:

$$
\tau_{xx} = 2\mu \frac{\partial u}{\partial x} - \frac{2}{3}\mu \left( \frac{\partial u}{\partial x} + \frac{\partial v}{\partial y} + \frac{\partial w}{\partial z} \right), \quad \tau_{xy} = \mu \left( \frac{\partial u}{\partial y} + \frac{\partial v}{\partial x} \right), \quad \tau_{xz} = \mu \left( \frac{\partial u}{\partial z} + \frac{\partial w}{\partial x} \right);
$$
$$
\tau_{yy} = 2\mu \frac{\partial v}{\partial y} - \frac{2}{3}\mu \left( \frac{\partial u}{\partial x} + \frac{\partial v}{\partial y} + \frac{\partial w}{\partial z} \right), \quad \tau_{yz} = \mu \left( \frac{\partial v}{\partial z} + \frac{\partial w}{\partial y} \right), \quad \tau_{zz} = 2\mu \frac{\partial w}{\partial z} - \frac{2}{3}\mu \left( \frac{\partial u}{\partial x} + \frac{\partial v}{\partial y} + \frac{\partial w}{\partial z} \right), \quad (5)
$$

in which $\mu$ is the fluid molecular viscosity.

The frozen components of the Fourier-heat-flux vector, which consider only thermal conduction, are defined by:

$$
q_{f,x} = -k_f \frac{\partial T}{\partial x}, \quad q_{f,y} = -k_f \frac{\partial T}{\partial y} \quad \text{and} \quad q_{f,z} = -k_f \frac{\partial T}{\partial z}, \quad (6)
$$

where $k_f$ is the mixture frozen thermal conductivity. The vibrational components of the Fourier-heat-flux vector are calculated as follows:

$$
q_{v,x} = -k_v \frac{\partial T_v}{\partial x}, \quad q_{v,y} = -k_v \frac{\partial T_v}{\partial y} \quad \text{and} \quad q_{v,z} = -k_v \frac{\partial T_v}{\partial z}, \quad (7)
$$

in which $k_v$ is the vibrational thermal conductivity and $T_v$ is the vibrational temperature, what characterizes this model as of two temperatures: translational/rotational and vibrational.

The terms of species diffusion, defined by the Fick law, to a condition of thermal non-equilibrium, are determined by ([31]):

$$\rho_s v_{sx} = -\rho D_s \frac{\partial Y_{MF,s}}{\partial x}, \ \rho_s v_{sy} = -\rho D_s \frac{\partial Y_{MF,s}}{\partial y}, \ \rho_s v_{sz} = -\rho D_s \frac{\partial Y_{MF,s}}{\partial z} \tag{8}$$

with "s" referent to a given species, $Y_{MF,s}$ being the molar fraction of the species, defined as:

$$Y_{MF,s} = \frac{\rho_s/M_s}{\sum_{k=1}^{ns} \rho_k/M_k} \tag{9}$$

and $D_s$ is the species-effective-diffusion coefficient.

The diffusion terms $\phi_x$, $\phi_y$ and $\phi_z$ which appear in the energy equation are defined by ([29]):

$$\phi_x = \sum_{s=1}^{ns} \rho_s v_{sx} h_s, \ \phi_y = \sum_{s=1}^{ns} \rho_s v_{sy} h_s, \ \phi_z = \sum_{s=1}^{ns} \rho_s v_{sz} h_s, \tag{10}$$

being $h_s$ the specific enthalpy (sensible) of the chemical species "s". Details of the calculation of the specific enthalpy, see [32]. The molecular diffusion terms calculated at the vibrational temperature, $\phi_{v,x}$, $\phi_{v,y}$ and $\phi_{v,z}$, which appear in the vibrational-internal-energy equation are defined by ([31]):

$$\phi_{v,x} = \sum_{s=mol} \rho_s v_{sx} h_{v,s}, \ \phi_{v,y} = \sum_{s=mol} \rho_s v_{sy} h_{v,s}, \ \phi_{v,z} = \sum_{s=mol} \rho_s v_{sz} h_{v,s}, \tag{11}$$

with $h_{v,s}$ being the specific enthalpy (sensible) of the chemical species "s" calculated at the vibrational temperature $T_v$. The sum of Eq. (11), as also those present in Eq. (4), considers only the molecules of the system, namely: $N_2$, $O_2$, $NO$, and $NO^+$.

The thermodynamic model, the transport model and the chemical models, as also the geometrical description of the spatial domain, are presented in [33-34].

# 3. MUSCL Procedure

A detailed description of the present implementation of the MUSCL procedure, as well the incorporation of TVD properties to the schemes, can be found in [14]. The expressions to calculate the fluxes following a MUSCL procedure and the nonlinear flux limiter definitions employed in the present work, which incorporates TVD properties, are defined as follows.

The conserved variables at the interface (i+1/2,j,k) can be considered as resulting from a combination of backward and forward extrapolations. To a linear one-sided extrapolation at the interface between the averaged values at the two upstream cells (i,j,k) and (i-1,j,k), one has:

$$Q_{i+1/2,j,k}^{L} = Q_{i,j,k} + \frac{\varepsilon}{2} \left( Q_{i,j,k} - Q_{i-1,j,k} \right), \text{ cell (i,j,k);} \tag{12}$$

$$Q^R_{i+1/2,j,k} = Q_{i+1,j,k} - \frac{\varepsilon}{2}\left(Q_{i+2,j,k} - Q_{i+1,j,k}\right), \text{ cell (i-1,j,k),} \tag{13}$$

leading to a second order fully one-sided scheme. If the first order scheme is defined by the numerical flux

$$F_{i+1/2,j,k} = F\left(Q_{i,j,k}, Q_{i+1,j,k}\right) \tag{14}$$

the second order space accurate numerical flux is obtained from

$$F^{(2)}_{i+1/2,j,k} = F\left(Q^L_{i+1/2,j,k}, Q^R_{i+1/2,j,k}\right). \tag{15}$$

Higher order flux vector splitting methods, such as those studied in this work, are obtained from:

$$F^{(2)}_{i+1/2,j,k} = F^+\left(Q^L_{i+1/2,j,k}\right) + F^-\left(Q^R_{i+1/2,j,k}\right). \tag{16}$$

All second order upwind schemes necessarily involve at least five mesh points or cells.

To reach high order solutions without oscillations around discontinuities, nonlinear limiters are employed, replacing the term $\varepsilon$ in Eqs. (12) and (13) by these limiters evaluated at the left and at the right states of the flux interface. To define such limiters, it is necessary to calculate the ratio of consecutive variations of the conserved variables. These ratios are defined as follows:

$$r^+_{i-1/2,j,k} = \left(Q_{i+1,j,k} - Q_{i,j,k}\right)/\left(Q_{i,j,k} - Q_{i-1,j,k}\right), \ r^+_{i+1/2,j,k} = \left(Q_{i+2,j,k} - Q_{i+1j,k}\right)/\left(Q_{i+1,j,k} - Q_{i,j,k}\right), \tag{17}$$

where the nonlinear limiters at the left and at the right states of the flux interface are defined by $\Psi^L = \Psi\left(r^+_{i-1/2,j,k}\right)$ and $\Psi^R = \Psi\left(1/r^+_{i+1/2,j,k}\right)$. In this work, five options of nonlinear limiters were considered to the numerical experiments. These limiters are defined as follows:

$$\Psi^{VL}_l(r_l) = \frac{r_l + |r_l|}{1 + r_l}, \text{ [35] limiter;} \tag{18}$$

$$\Psi^{VA}_l(r_l) = \frac{r_l + r_l^2}{1 + r_l^2}, \text{ Van Albada limiter;} \tag{19}$$

$$\Psi^{MIN}_l(r_l) = \text{signal}_l \text{MAX}\left(0, \text{MIN}\left(|r_l|, \text{signal}_l\right)\right), \text{ minmod limiter;} \tag{20}$$

$$\Psi^{SB}_l(r_l) = \text{MAX}\left(0, \text{MIN}(2r_l, 1), \text{MIN}(r_l, 2)\right), \text{ "Super Bee" limiter, due to [36];} \tag{21}$$

$$\Psi^{\beta-L}_l(r_l) = \text{MAX}\left(0, \text{MIN}(\beta r_l, 1), \text{MIN}(r_l, \beta)\right), \text{ $\beta$-limiter,} \tag{22}$$

with "l" varying from 1 to 12 (three-dimensional space), $\text{signal}_l$ being equal to 1.0 if $r_l \geq 0.0$ and -1.0 otherwise, $r_l$ is the ratio of consecutive variations of the $l^{th}$ conserved variable, and $\beta$ is a parameter assuming values between 1.0 and 2.0, being 1.5 the value assumed in this work. Only the minmod solutions are presented in this work. With the implementation of the numerical flux vectors following this MUSCL procedure, second order spatial accuracy and TVD properties are incorporated in the algorithms.

## 4. ENO Procedure

ENO schemes overcome the limitations of TVD schemes by relaxing the requirement of total variation non-increasing ([11]). They are conservative, essentially non-oscillatory and give uniform accuracy in smooth regions, without the degradation of accuracy at non-sonic local extrema as observed with TVD methods. There are several possible approaches when constructing ENO schemes. [17] use the ENO scheme to construct a higher order solution to the cell-average of the conservation equation using a sliding average. The ENO scheme of [17], therefore, gives an r-th order accurate approximation to the cell averages. According to [17], the ENO schemes can be expressed as:

$$\overline{E}_h(\tau) \bullet \overline{Q} \equiv A_h \bullet E(\tau) \bullet \text{Re}\,c(\overline{Q}),$$ (23)

where:

$\overline{E}_h(\tau) \bullet \overline{Q}$ is the new ENO scheme applied to the cell average solution;

$A_h$ is the cell averaging operator;

$E(\tau)$ is the exact evolution operator (the solver);

$\text{Re}\,c(\overline{Q})$ is the reconstruction operator;

$\overline{Q}$ is the average solution.

The most important ingredient of their ENO method is the reconstruction of the point values Q(x,y,z) from the cell averaged values $\overline{Q}_{i,j,k}$. These point values are necessary to compute the flux at the cell faces. This is done with a reconstruction method that is conservative, essentially non-oscillatory and gives at all points in a neighborhood around $(x_i,y_i,z_i)$ an r-th order approximation to Q, when Q is smooth. This formulation is employed in the present work.

The implementation of the [25-26] schemes in the ENO method of [17], which uses a reconstruction from the cell averaged variables, is straightforward. The first step in the ENO reconstruction is the determination of the cell averaged variables. In the present work, it was adopted that the averaged operator is the identity operator; hence, the averaged variables are exactly the conserved variable at the cell point. A higher order polynomial representation of Q in each cell is now constructing. In this work, it can be by Newton interpolation or Hermite interpolation. The values at the left and right side of the cell, as in the MUSCL case, are now used in the [25-26] solvers.

## 5. Newton Interpolation

A higher order polynomial representation of Q in each cell can be constructed by determining the divided differences used in the Newton interpolation method using the following recursive algorithm: Considering the $\xi$ direction, the divided differences are calculated as follows:

$$H_0[\xi_{i,j,k}] = Q(\xi_{i,j,k}) = Q_{i,j,k} ; \; H_1[\xi_{i+1,j,k}] = Q(\xi_{i+1,j,k}) = Q_{i+1,j,k} ;$$ (24)

$$H_{00}[\xi_{i,j,k},\xi_{i+1,j,k}] = \left[H_1(\xi_{i+1,j,k}) - H_0(\xi_{i,j,k})\right]/\left(\xi_{i+1,j,k} - \xi_{i,j,k}\right);$$ (25)

$$H_{000}[\xi_{i,j,k},\xi_{i+1,j,k},\xi_{i+2,j,k}] = \left\{H_{01}\left[\xi_{i+1,j,k},\xi_{i+2,j,k}\right] - H_{00}\left[\xi_{i,j,k},\xi_{i+1,j,k}\right]\right\}/\left(\xi_{i+2,j,k} - \xi_{i,j,k}\right);$$ (26)

If the divided difference $H_{000}[\xi_{i,j,k}, \xi_{i+1,j,k}, \xi_{i+2,j,k}]$ is larger than $H_{001}[\xi_{i+1,j,k}, \xi_{i+2,j,k}, \xi_{i+3,j,k}]$, the choice should be $H_{000} = H_{001}[\xi_{i+1,j,k}, \xi_{i+2,j,k}, \xi_{i+3,j,k}]$; on the contrary, $H_{000}[\xi_{i,j,k}, \xi_{i+1,j,k}, \xi_{i+2,j,k}]$ is accepted. This process is repeated until the required order of the interpolation is obtained and applied to each component of Q independently. Note that the calculated stencil is computed dynamically at each point and is non-linear in nature. With the choice of the minimum divided difference at a point, the best molecule is determined to provide high accuracy.

After the determination of the coefficients of the Newton polynomial, the reconstruction process is finished:

$$\text{Rec}(\overline{Q}, \xi) = Q(\xi_{i,j,k}) + H_0(\xi - \xi_{i,j,k}) + H_{00}(\xi - \xi_{i,j,k})(\xi - \xi_{i+1,j,k}) + H_{000}(\xi - \xi_{i,j,k})(\xi - \xi_{i+1,j,k})(\xi - \xi_{i+2,j,k}) + \dots \quad (27)$$

This process gives a representation of the solution in each cell and can be used to determine the values of Q at the cell faces. Observe that the reconstruction process results in a polynomial of order m-th to the vector of conserved variables as function of the generalized coordinate $\xi$. The same reasoning is applied to the $\eta$ and $\zeta$ directions.

## 6. Hermite Interpolation

If $f \in C[a,b]$ and $\xi_0, \dots, \xi_n \in [a,b]$ are distincts, the unique polynomial of least degree agreeing with f and f' at $\xi_0, \dots, \xi_n$ is the Hermite polynomial of degree at most 2n+1 given by

$$\text{Rec}(\overline{Q}, \xi) = \sum_{j=0}^{n} f(\xi_j) H_{n,j}(\xi) + \sum_{j=0}^{n} f'(\xi_j) \hat{H}_{n,j}(\xi), \quad (28)$$

where

$$H_{n,j}(\xi) = \left[1 - 2(\xi - \xi_j) L'_{n,j}(\xi_j)\right] L^2_{n,j}(\xi) \quad (29)$$

and

$$\hat{H}_{n,j}(\xi) = (\xi - \xi_j) L^2_{n,j}(\xi). \quad (30)$$

In this context, $L_{n,j}(\xi)$ denotes the $j^{th}$ Lagrange coefficient polynomial of degree n. Moreover, if $f \in C^{2n+2}[a,b]$, then

$$f(\xi) = H_{2n+1}(\xi) + \frac{(\xi - \xi_0)^2 \dots (\xi - \xi_n)^2}{(2n+2)!} f^{(2n+2)}(\chi) \quad (31)$$

for some $\chi$ with $a < \chi < b$. In addition, since the first derivatives of the Hermite polynomial agree with those of f, it has the same "shape" as the function at $[\xi_i, f(\xi_i)]$ in the sense that the tangent lines to the polynomial and to the function agree.

The first derivative of the function f, which is our vector of conserved variables Q, is determined by the first divided difference of Q in relation to $\xi$, $\eta$ or $\zeta$, depending of the spatial direction under study. For j varying from 0 to n, the first derivative in the second sum of Eq. (28) is adopted as the minimum value of the first derivatives in this interval.

## 7. WENO Procedure

The present WENO formulation is based on the work of [24]. The WENO procedure consists to approximate the Q contribution from each cell by the negative and positive contributions from adjacent cells. These negative and positive contributions are determined considering weight coefficients to balance the influence of each cell. Considering only one spatial subscript to easy understanding, one has:

$$Q^- = \sum_{r=0}^{k-1} \omega_r Q^{-(r)} \text{ and } Q^+ = \sum_{r=0}^{k-1} \overline{\omega}_r Q^{+(r)} \,, \tag{32}$$

where:

$$Q^{-(r)} = \sum_{j=0}^{k-1} c_{rj} \overline{Q}_{i-r+j} \quad \text{and} \quad Q^{+(r)} = \sum_{j=0}^{k-1} \overline{c}_{rj} \overline{Q}_{i-r+j} \,, \tag{33}$$

with $c_{rj}$ and $\overline{c}_{rj}$ being constants, and $\overline{Q}$ being the polynomial reconstruction function of the ENO scheme, obtained by Newton interpolation procedure.

It is important to emphasize that for a third-order WENO scheme, a second order polynomial reconstruction function should be used, and for a fifth-order WENO scheme, a third order polynomial function should be prescribed. Another point is that the $Q^-$ and $Q^+$ functions, from the surrounding cells around the (i,j,k) cell, contribute to the Q function from the following form:

"*Q receives $Q^-$ from the i+1 cell to the i+1/2 interface and receives $Q^+$ from the i-1 cell to the i-1/2 interface.*"

To a third-order WENO procedure, one has in Table 1 the following values to $c_{rj}$ and its associated vector of conserved variables to the determination of $Q^-$. Remembering that, in this case, k = 2 which implies a third-order WENO procedure.

The weighting coefficients $\omega_r$, which are 2k-1 accurate, are described by Eq. (34):

$$\omega_r = \frac{\alpha_r}{\sum_{s=0}^{k-1} \alpha_s} \,, \text{ and } \alpha_r = \frac{d_r}{\left(\varepsilon + \beta_r\right)^2} \,, \tag{34}$$

where:

$\varepsilon = 10^{-6}$, with r varying from 0 to 1;
$d_0 = 2/3$, and $d_1 = 1/3$;

$$\beta_0 = \left(\overline{Q}_{i+1} - \overline{Q}_i\right)^2 \,, \ \beta_1 = \left(\overline{Q}_i - \overline{Q}_{i-1}\right)^2 . \tag{35}$$

The parameter $\varepsilon$, presented in Eq. (34), is used to avoid zero value to the denominator. The $\beta_r$ terms are the so-called "smooth indicators" of the stencil $S_r$.

To $Q^+$ determination, one needs the values of $\overline{c}_{rj}$ and $\overline{Q}$, defined in Table 2. Note that $\overline{c}_{rj} = c_{r-1j}$. The weighting coefficient $\overline{\omega}_r$ is determined by Eq. (36):

$$\overline{\omega}_r = \frac{\overline{\alpha}_r}{\displaystyle\sum_{s=0}^{k-1}\overline{\alpha}_s}, \text{ and } \overline{\alpha}_r = \frac{\overline{d}_r}{\left(\varepsilon + \beta_r\right)^2}; \tag{36}$$

where $\varepsilon$ and $\beta_r$ are defined as aforementioned and $\overline{d}_r = d_{k-1-r}$. Hence, one has: $\overline{d}_0 = d_1 = 1/3$, and $\overline{d}_1 = d_0 = 2/3$. Fig. 1 shows a schematic of the $Q^-$ and $Q^+$ contributions to cell (i,j,k).

To k = 3, which implies a fifth-order WENO procedure, r varies from 0 to 2. The values of $c_{rj}$ and $\overline{Q}$ are seen in Table 3.

The values of $d_r$, in Eq. (34) are: $d_0 = 3/10$, $d_1 = 3/5$, and $d_2 = 1/10$. The expressions to the smooth indicators are:

$$\beta_0 = \frac{13}{12}\left(\overline{Q}_i - 2\overline{Q}_{i+1} + \overline{Q}_{i+2}\right)^2 + \frac{1}{4}\left(3\overline{Q}_i - 4\overline{Q}_{i+1} + \overline{Q}_{i+2}\right)^2; \tag{37}$$

$$\beta_1 = \frac{13}{12}\left(\overline{Q}_{i-1} - 2\overline{Q}_i + \overline{Q}_{i+1}\right)^2 + \frac{1}{4}\left(\overline{Q}_{i-1} - \overline{Q}_{i+1}\right)^2; \tag{38}$$

$$\beta_2 = \frac{13}{12}\left(\overline{Q}_{i-2} - 2\overline{Q}_{i-1} + \overline{Q}_i\right)^2 + \frac{1}{4}\left(\overline{Q}_{i-2} - 4\overline{Q}_{i-1} + 3\overline{Q}_i\right)^2. \tag{39}$$

To $Q^+$, one has the values of $\overline{c}_{rj}$ and $\overline{Q}$, defined in Table 4. The values of $\overline{d}_r$ are given by: $\overline{d}_0 = d_2 = 1/10$, $\overline{d}_1 = d_1 = 3/5$, and $\overline{d}_2 = d_0 = 3/10$. With the application of Eq. (36), the $\overline{\omega}_r$ coefficients are calculated and the $Q^-$ and $Q^+$ functions are defined, Eqs. (32-33).

## 8. Numerical Algorithms

Considering the simulation of a three-dimensional and structured case, the numerical algorithms follow the formulation described in [33]. The system is solved in three parts separately, according to [37]. Hence, the discrete-dynamic-convective flux is given by:

$$R_{i+1/2,j,k} = \left|S\right|_{i+1/2,j,k}\left\{\frac{1}{2}M_{i+1/2,j,k}\left[\begin{pmatrix}\rho a \\ \rho au \\ \rho av \\ \rho aw \\ \rho aH\end{pmatrix}_L + \begin{pmatrix}\rho a \\ \rho au \\ \rho av \\ \rho aw \\ \rho aH\end{pmatrix}_R\right] - \frac{1}{2}\phi_{i+1/2,j,k}\left[\begin{pmatrix}\rho a \\ \rho au \\ \rho av \\ \rho aw \\ \rho aH\end{pmatrix}_R - \begin{pmatrix}\rho a \\ \rho au \\ \rho av \\ \rho aw \\ \rho aH\end{pmatrix}_L\right]\right\} + \begin{pmatrix}0 \\ S_x p \\ S_y p \\ S_z p \\ 0\end{pmatrix}_{i+1/2,j,k}, \tag{40}$$

the discrete-chemical-convective flux is defined by:

$$R_{i+1/2,j,k} = |S||_{i+1/2,j,k} \left\{ \frac{1}{2} M_{i+1/2,j,k} \left[ \begin{pmatrix} \rho_1 a \\ \rho_2 a \\ \rho_4 a \\ \rho_5 a \\ \rho_6 a \\ \rho_7 a \end{pmatrix}_L + \begin{pmatrix} \rho_1 a \\ \rho_2 a \\ \rho_4 a \\ \rho_5 a \\ \rho_6 a \\ \rho_7 a \end{pmatrix}_R \right] - \frac{1}{2} \phi_{i+1/2,j,k} \left[ \begin{pmatrix} \rho_1 a \\ \rho_2 a \\ \rho_4 a \\ \rho_5 a \\ \rho_6 a \\ \rho_7 a \end{pmatrix}_R - \begin{pmatrix} \rho_1 a \\ \rho_2 a \\ \rho_4 a \\ \rho_5 a \\ \rho_6 a \\ \rho_7 a \end{pmatrix}_L \right] \right\}, \quad (41)$$

and the discrete-vibrational-convective flux is determined by:

$$R_{i+1/2,j,k} = |S||_{i+1/2,j,k} \left\{ \frac{1}{2} M_{i+1/2,j,k} \left[ (\rho e_v a)_L + (\rho e_v a)_R \right] - \frac{1}{2} \phi_{i+1/2,j,k} \left[ (\rho e_v a)_R - (\rho e_v a)_L \right] \right\}. \quad (42)$$

The same definitions presented in [33] are valid to this algorithm. The time integration is performed employing the Euler backward method, first-order accurate in time, to the three types of convective flux. To the dynamic part, this method can be represented in general form by:

$$Q_{i,j,k}^{(n+1)} = Q_{i,j,k}^{(n)} - \left( \Delta t_{i,j,k} / V_{i,j,k} \right) \times R \left( Q_{i,j,k}^{(n)} \right), \quad (43)$$

to the chemical part, it can be represented in general form by:

$$Q_{i,j,k}^{(n+1)} = Q_{i,j,k}^{(n)} - \Delta t_{i,j,k} \times \left[ R \left( Q_{i,j,k}^{(n)} \right) / V_{i,j,k} - S_C \left( Q_{i,j,k}^{(n)} \right) \right], \quad (44)$$

where the chemical source term $S_C$ is calculated with the rate controlling temperature (Defined in [33]). Finally, to the vibrational part,

$$Q_{i,j,k}^{(n+1)} = Q_{i,j,k}^{(n)} - \Delta t_{i,j,k} \left[ R \left( Q_{i,j,k}^{(n)} \right) / V_{i,j,k} - S_v \left( Q_{i,j,k}^{(n)} \right) \right], \quad (45)$$

in which:

$$S_v = \sum_{s=mol} q_{T-V,s} + \sum_{s=mol} S_{C,s} e_{v,s}. \quad (46)$$

The definition of the dissipation term $\phi$ determines the particular formulation of the convective fluxes. The choice below corresponds to the [25] scheme, according to [38]:

$$\phi_{i+1/2,j,k} = \phi_{i+1/2,j,k}^{VL} = \begin{cases} |M_{i+1/2,j,k}|, & \text{if } |M_{i+1/2,j,k}| \geq 1; \\ |M_{i+1/2,j,k}| + 0.5(M_R - 1)^2, & \text{if } 0 \leq M_{i+1/2,j,k} < 1; \\ |M_{i+1/2,j,k}| + 0.5(M_L + 1)^2, & \text{if } -1 < M_{i+1/2,j,k} \leq 0; \end{cases} \quad (47)$$

and the choice below corresponds to the [26] scheme, according to [38]:

$$\phi_{i+1/2,j,k} = \phi_{i+1/2,j,k}^{LS} = |M_{i+1/2,j,k}|. \quad (48)$$

This scheme is first-order accurate in space and in time. The high-order spatial accuracy is obtained by the MUSCL procedure, by the ENO procedure or by the WENO procedure. These procedures are described in the previous sections.

The viscous formulation has been provided in [39], which adopts the Green theorem to calculate primitive variable gradients. The viscous vectors are obtained by arithmetical average between cell (i,j,k) and its neighbors. As was done with the convective terms, there is a need to separate the viscous flux in three parts: dynamical viscous flux, chemical viscous flux and vibrational viscous flux. The dynamical part corresponds to the first five equations of the Navier-Stokes ones, the chemical part corresponds to the following six equations, and the vibrational part corresponds to the last equation.

# 9. Physical Problem, Meshes, and Initial Condition

The flow around a blunt body problem is studied in the present work. The analyzed geometry is a blunt body with 1.0m of nose ratio and parallel rectilinear walls. The far field is located at 20.0 times the nose ratio in relation to the configuration nose.

It is important to emphasize that the present work is directed to the academic public and because it an educational problem was chosen to study, not regarding the complexity features of industrial applications. However, the theory can also be applied to the industrial sector.

Fig. 2 shows the inviscid mesh used to the blunt body problem when Euler equations are been solved. This mesh is composed of 22,932 rectangular cells and 26,500 nodes. The equivalent finite differences mesh has 53x50x10 points. A "O" mesh has been taken as the base to construct such mesh. No smoothing is used in this mesh generation process, which has been constructed in Cartesian coordinates. On the other hand, the viscous mesh is shown in Fig. 3, which is composed of the same number of cells and nodes, employing, however, an exponential stretching of 5.0% in the η direction. The initial condition is shown in Table 5. The Reynolds number is estimated by [40].

# 10. Results

Tests were performed in a Core i7 processor of 1.9 GHz and 6.0Gbytes of RAM microcomputer in a Windows 8.1 environment. Three (3) orders of reduction of the maximum residual in the field were considered to obtain a converged solution. The residual was defined as the value of the discretized conservation equation. The entrance or attack angle and the longitudinal angle were adopted equal to zero.

## 10.1 Inviscid Case

*Five Species Results.* Figs. 4 and 5 presents the pressure contours obtained by the [25-26] algorithms, respectively, as using the MUSCL procedure to obtain high resolution in the inviscid case. Both solutions present good symmetry features. The pressure field generated by the [25] algorithm is more severe than that obtained by the [26] algorithm. The most critical stagnation pressure between solutions is achieved by the [26] algorithm.

Figs. 6 to 16 exhibit the pressure contours obtained by the [25-26] algorithms as using the ENO procedure in its Newton and Hermite interpolations to obtain high resolution in the inviscid case. Good symmetry aspects are observed in all solutions. The shock wave is well captured by both schemes. The most severe pressure field is obtained by the [25] algorithm as using the ENO procedure with the Newton interpolation. In this case, the biggest stagnation pressure is obtained by the 4th-order variant of the ENO procedure, although the best estimative for the theoretical value is due to the 5th-order variant.

It is interesting to note that the Newton interpolation solutions are always better than the Hermite interpolation solutions, as emphasized in [41].

Figs. 17 and 18 present the pressure contours obtained by the [25-26] numerical algorithms as using the WENO procedure to obtain high resolution in the inviscid case. The WENO procedure in its 5th-order variant did not present converged results. The shock wave is better captured by the [25] algorithm, although good symmetry aspects are observed in both solutions. The most severe pressure field in this case is obtained by the [25] algorithm. The biggest stagnation pressure is also due to the [25] algorithm, although inferior enough in relation to the theoretical value of this parameter.

In a global analysis for this inviscid case, the most severe pressure field is due to the [25] algorithm as using the ENO procedure and Newton interpolation in its 4th-order variant, although the most correct value of the stagnation pressure, as will be seen, is due to its 5th-order variant.

***Seven Species Results.*** Figs. 19 and 20 presents the pressure contours obtained by the [25-26] algorithms, respectively, as using the MUSCL procedure to obtain high resolution in the inviscid case. Both solutions present good symmetry features. The pressure field generated by the [26] algorithm is more severe than that obtained by the [25] algorithm. The most critical stagnation pressure between solutions is achieved by the [26] algorithm.

Figs. 21 to 30 exhibit the pressure contours obtained by the [25-26] algorithms as using the ENO procedure in its Newton and Hermite interpolations to obtain high resolution in the inviscid case. Good symmetry aspects are observed in all solutions. The shock wave is well captured by both schemes. The most severe pressure field is obtained by the [25] algorithm as using the ENO procedure with the Newton interpolation. In this case, the biggest stagnation pressure is obtained by the 4th-order variant of the ENO procedure, although the best estimative for the theoretical value is again due to the 5th-order variant.

It is again interesting to note that the Newton interpolation solutions are always better than the Hermite interpolation solutions, as previously discussed in [41].

Figs. 31 and 32 present the pressure contours obtained by the [25-26] numerical algorithms as using the WENO procedure to obtain high resolution in the inviscid case. The WENO procedure in its 5th-order variant did not present converged results. The shock wave is better captured by the [25] algorithm, although good symmetry aspects are observed in both solutions. The most severe pressure field in this case is obtained by the [25] algorithm. The biggest stagnation pressure of the WENO solutions is also due to the [25] algorithm, although inferior enough in relation to the theoretical value of this parameter.

In an overall analysis for this inviscid case, the most severe pressure field is due to the [25] algorithm as using the ENO procedure and Newton interpolation in its 4th-order variant, although the most correct value of the stagnation pressure is again due to its 5th-order variant.

## 10.2 Viscous Case

***Five Species Results.*** Fig. 33 shows the pressure contours obtained by the [25] scheme as using the MUSCL procedure to obtain high resolution in the viscous case. The [26] algorithm did not present converged results. Good symmetry characteristics are observed in this solution. The stagnation pressure is reasonable predicted.

Figs. 34 to 36 exhibit the pressure contours obtained by the [25-26] algorithms as using the ENO procedure with Newton interpolation to obtain high resolution in this viscous case. Only the Newton interpolation to 3rd- and 4th-orders of accuracy has presented converged results. The WENO procedure did not present converged results too. The most severe pressure field is due to the [26] algorithm as using the ENO procedure in its 4th-order variant. The most correct stagnation pressure value is due to the [25] algorithm using Newton interpolation to 4th-order.

A comprehensive analysis for this viscous case showed that the most severe pressure field is captured by the [26] algorithm as using the ENO procedure and Newton interpolation in its 4th-order variant, although the best prediction of the stagnation pressure in this case is due to the [25] algorithm using the same procedure and interpolation method.

***Seven Species Results.*** Fig. 37 shows the pressure contours obtained by the [25] algorithm as using the MUSCL procedure to obtain high resolution in the viscous case. The [26] algorithm did not present converged results. Good symmetry characteristics are observed in this solution. The stagnation pressure is reasonable predicted.

Figs. 38 to 40 exhibit the pressure contours obtained by the [25-26] algorithms as using the ENO procedure with Newton interpolation to obtain high resolution in this viscous case. Only the Newton interpolation to 3rd- and 4th-orders of accuracy has presented converged results. The WENO procedure did not present converged results too. The most severe pressure field is due to the [26] algorithm as using the ENO procedure in its 4th-order variant. The most correct stagnation pressure value is due to the [25] algorithm using Newton interpolation to 4th-order.

The viscous case overall characteristics showed that the most severe pressure field is captured by the [26] algorithm as using the ENO procedure and Newton interpolation in its 4th-order variant, although the best prediction of the stagnation pressure in this case is due to the [25] algorithm using the same procedure and interpolation method.

Considering inviscid and viscous results, the most severe pressure field is due to the [26] algorithm in the viscous case. However, the best estimative of the stagnation pressure is due to [25] algorithm in the inviscid case, as expected. It is important to observe that the identification of the most severe pressure field is vital in terms of aerodynamic design of aerospace vehicles, which aims to highlight the most strength flight condition.

## 10.3 Quantitative Results

In terms of quantitative results, the present work compares the reactive results against the perfect gas solutions. The stagnation pressure at the blunt body nose was evaluated assuming the perfect gas formulation. Such parameter calculated at this way is not the best comparison, but in the absence of practical reactive results, this constitutes the best available result.

To calculate the stagnation pressure ahead of the blunt body, [42] presents in its B Appendix values of the normal shock wave properties ahead of the configuration. The ratio $pr_0/pr_\infty$ is estimated as function of the normal Mach number and the stagnation pressure $pr_0$ can be determined from this parameter. Hence, to a freestream Mach number of 9.0 (close to 8.78), the ratio $pr_0/pr_\infty$ assumes the value 104.8. The value of $pr_\infty$ is determined by the following expression:

$$pr_\infty = \frac{pr_{initial}}{\rho_\infty \times a_\infty^2}. \tag{49}$$

In the present study, $pr_{initial} = 687 N/m^2$, $\rho_\infty = 0.004 kg/m^3$ and $a_\infty = 317.024 m/s$. Considering these values, one concludes that $pr_\infty = 1.709$ (dimensionless). Using the ratio obtained from [42], the stagnation pressure ahead of the configuration nose is estimated as 179.10 unities. Tables 6 to 9 compare the values obtained from the simulations with this theoretical parameter and present the numerical percentage errors. The [25] results are shown in Table 6, whereas the [26] in Table 7 for the five species chemical model, and Table 8 presents the [25] results and Table 9 the [26] results for the seven species chemical model.

The best result was obtained with the ENO procedure in its 5th-order variant using Newton interpolation, in an inviscid case, as expected, with an error of 0.62% for the [25] algorithm using the seven species chemical

model. The second best estimative was obtained with the ENO procedure in its 2nd-order variant using Newton interpolation, also in an inviscid case, with an error of 0.84% for the [25] algorithm too as using both chemical models. It is important to note that considering the ENO procedure using the Newton interpolation, errors less than 3.00% were found with the [25] numerical algorithm in the inviscid case and less than 4.00% for the viscous case. Moreover, the Hermite interpolation solutions have presented errors inferior to 12.00% for the [25] algorithm. The best result with the [26] numerical algorithm was the ENO procedure using the 4th-order Newton interpolation, in a viscous case, with an error of 6.20% as using the seven species chemical model. The WENO procedure had a bad performance, yielding errors as large as 27.94% for the [25] algorithm using the five species model, and of 42.16% for the [26] algorithm using the seven species model.

## 10.4 Computational Performance

Tables 10 and 11 present the computational data of the [25] and the [26] algorithms for the blunt body problem as using the five species chemical model. It shows the CFL number and the number of iterations to convergence for all studied cases in the present work. As can be seen, all the cases used the same CFL number 0.010 and the best performance is due to the [25] algorithm as using the MUSCL procedure, converging in circa of 16,927 iterations. The best ENO performance was due to the 3rd-order Hermite variant, for the inviscid case, converging in 17,637 iterations. This result was obtained with the [25] algorithm. In relation to the [26] algorithm, the best performance was to the 5th-order Hermite variant, for the inviscid case, converging in 27,548 iterations.

Tables 12 and 13 present the computational data of the [25] and the [26] algorithms for the blunt body problem as using the seven species chemical model. It shows the CFL number and the number of iterations to convergence for all studied cases in the present work. As can be seen, all the cases used the same CFL number 0.010 and the best performance is due to the [25] algorithm as using the MUSCL procedure, converging in circa of 16,774 iterations. The best ENO performance was due to the 3rd-order Hermite variant, for the inviscid case, converging in 17,511 iterations. This result was obtained with the [25] algorithm. In relation to the [26] algorithm, the best performance was to the 5th-order Hermite variant, for the inviscid case, converging in 27,177 iterations.

As can be observed, the best procedure to obtain high order resolution is the ENO procedure employing the Newton interpolation process. The Hermite interpolation process present good computational performance; however, its numerical results are worse than the Newton ones. Such conclusion was obtained in [41] and confirmed in this work. The MUSCL approach is a good option if only 2nd-order precision is required. The WENO procedure has presented unsatisfactory results.
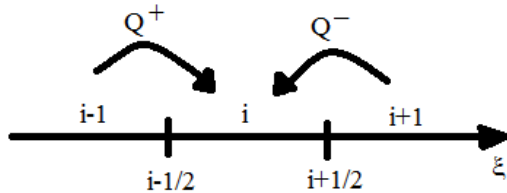

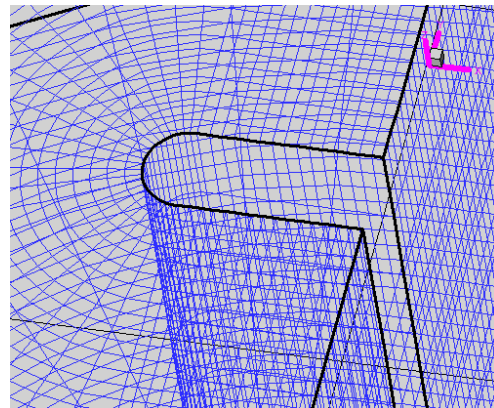
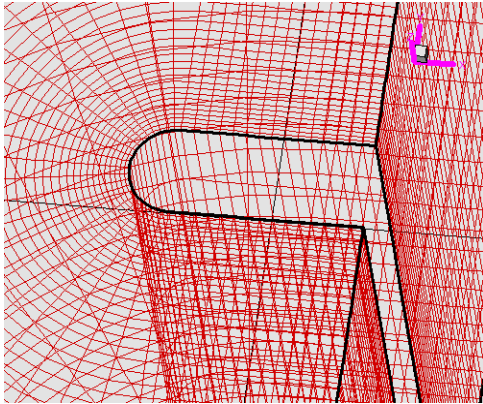**Fig. 1. Contributions of $Q^-$ and $Q^+$ to cell (i,j,k)**

**Fig. 2. Inviscid mesh**

Fig. 3. Viscous mesh

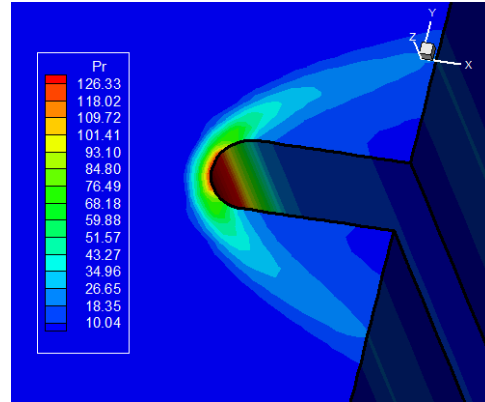**INVISCID CASE – FIVE SPECIES**



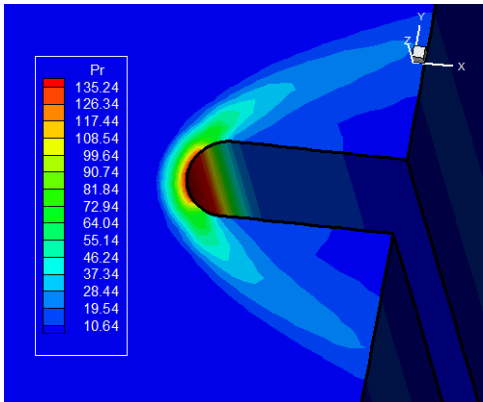Fig. 4. Pressure contours (MUSCL-2$^{nd}$-VL)



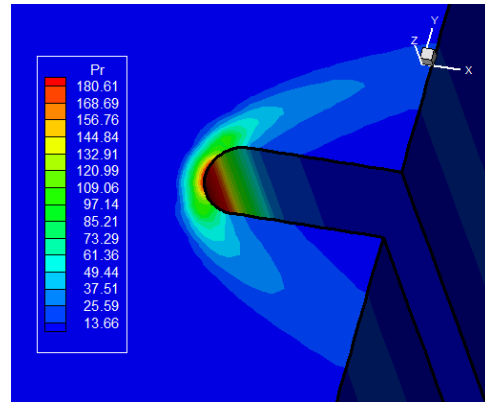Fig. 5 Pressure contours (MUSCL-2$^{nd}$-LS)



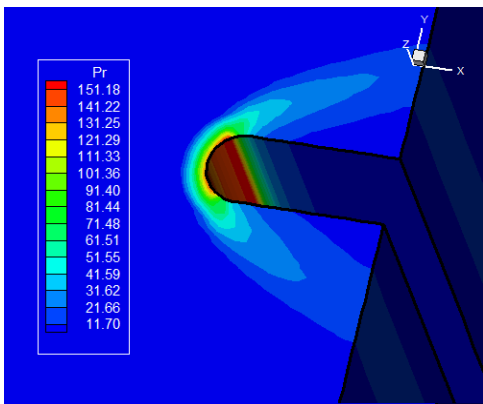Fig. 6. Pressure contours (ENO-NEWTON-2$^{nd}$-VL)
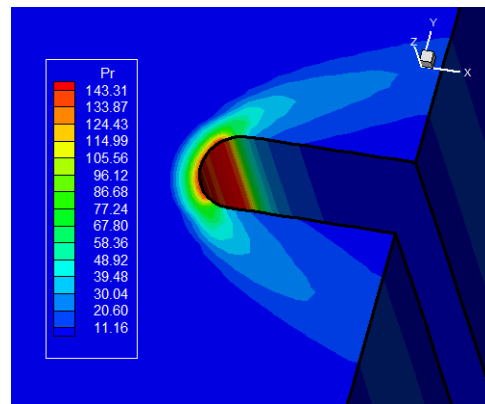


Fig. 7. Pressure contours (ENO-NEWTON-2$^{nd}$-LS)
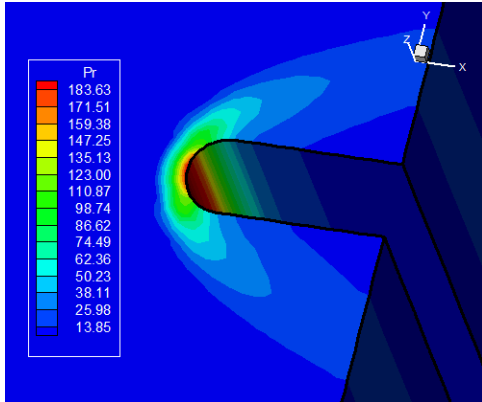


Fig. 8. Pressure contours (ENO-NEWTON-3$^{rd}$-LS)

**Fig. 9. Pressure contours (ENO-NEWTON-4$^{th}$-VL)**
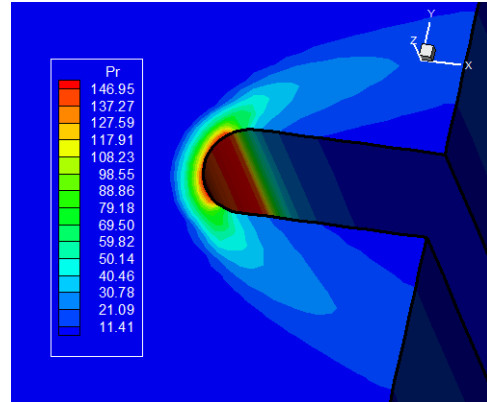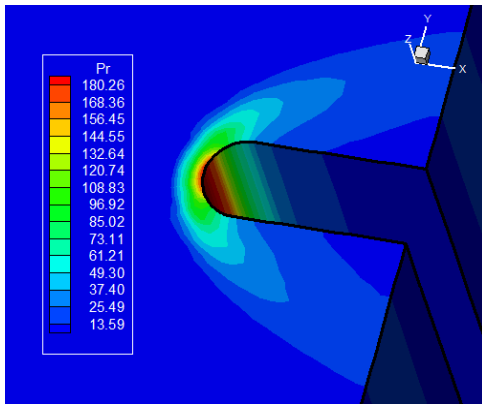


**Fig. 10. Pressure contours (ENO-NEWTON-4$^{th}$-LS)**



**Fig. 11. Pressure contours (ENO-NEWTON-5$^{th}$-VL)**
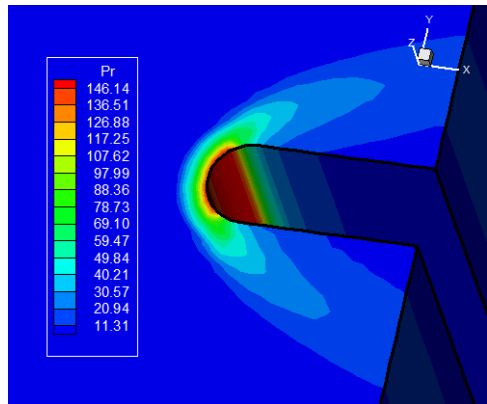


**Fig. 12. Pressure contours (ENO-NEWTON-5$^{th}$-LS)**
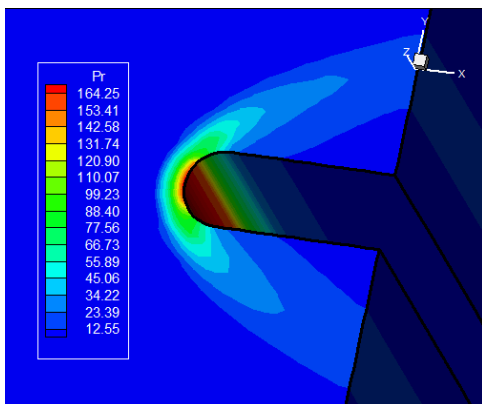


**Fig. 13. Pressure contours (ENO-HERMITE-3$^{rd}$-VL)**
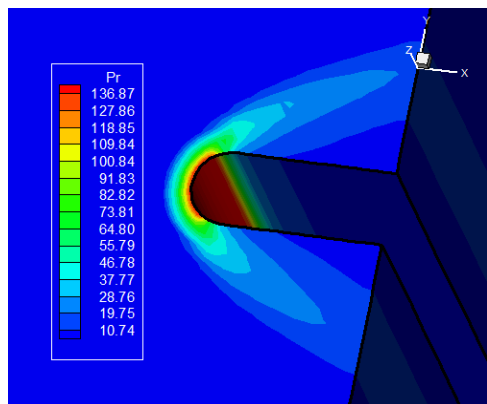


**Fig. 14. Pressure contours (ENO-HERMITE-3$^{rd}$-LS)**
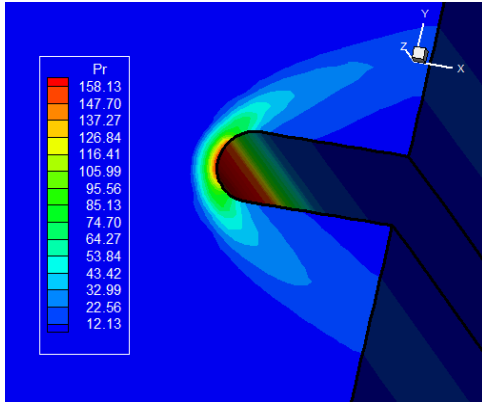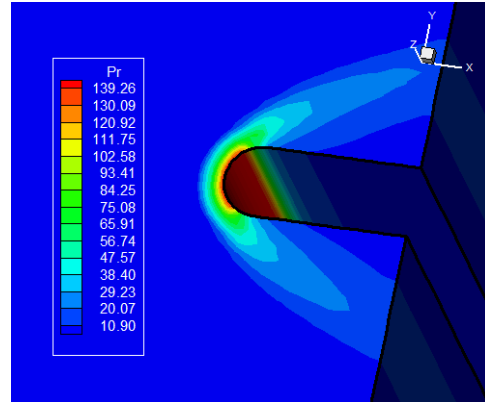
**Fig. 15. Pressure contours (ENO-HERMITE-5th-VL)**

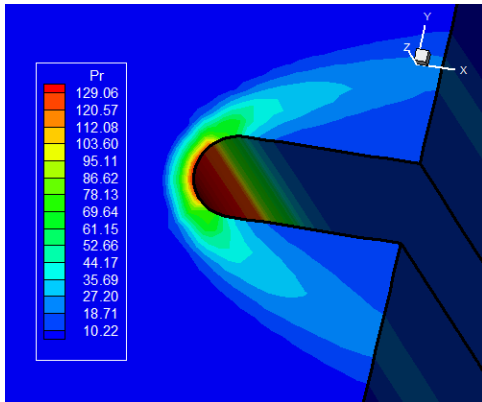**Fig. 16. Pressure contours (ENO-HERMITE-5th-LS)**



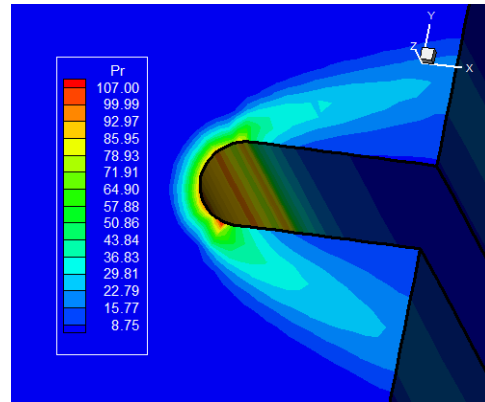**Fig. 17. Pressure contours (WENO-NEWTON-3rd-VL)**

**Fig. 18. Pressure contours (WENO-NEWTON-3rd-LS)**
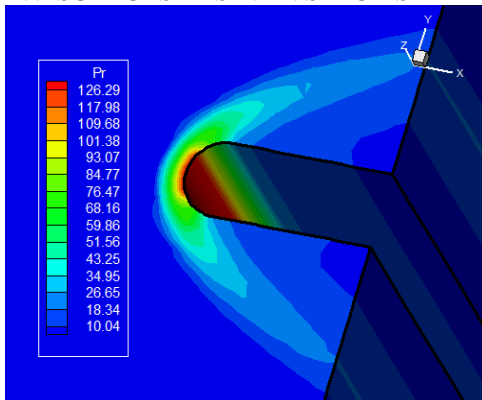
**INVISCID CASE – SEVEN SPECIES**
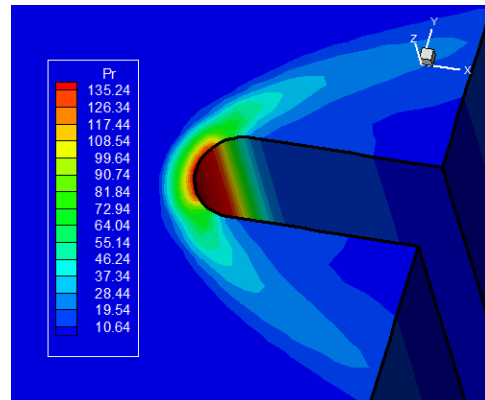


**Fig. 19. Pressure contours (MUSCL-2nd-VL)**

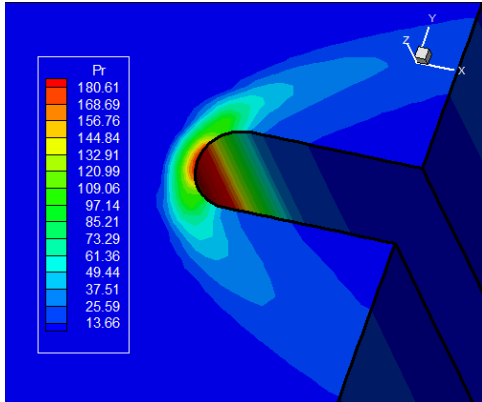**Fig. 20. Pressure contours (MUSCL-2nd-LS)**

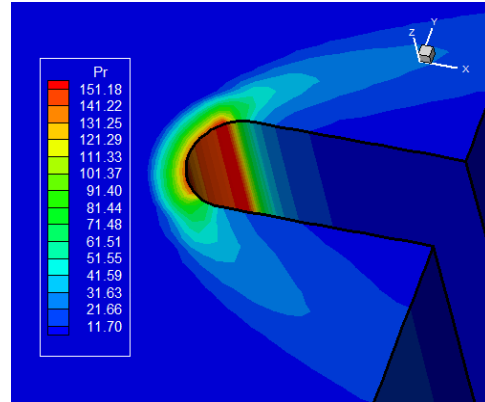**Fig. 21. Pressure contours (ENO-NEWTON-2nd-VL)**



**Fig. 22. Pressure contours (ENO-NEWTON-2nd-LS)**
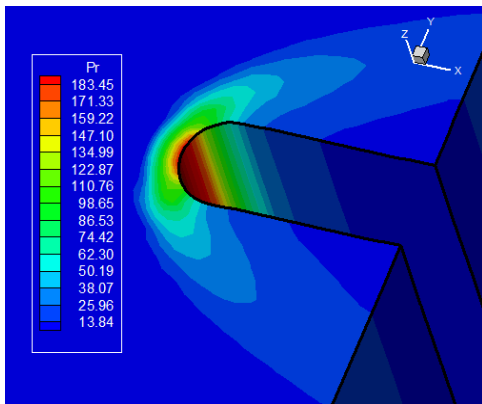


**Fig. 23. Pressure contours (ENO-NEWTON-4th-VL)**
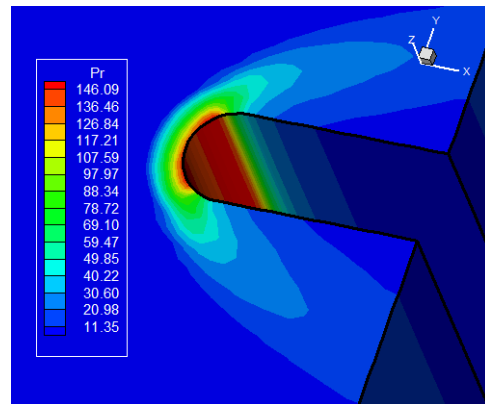


**Fig. 24. Pressure contours (ENO-NEWTON-4th-LS)**
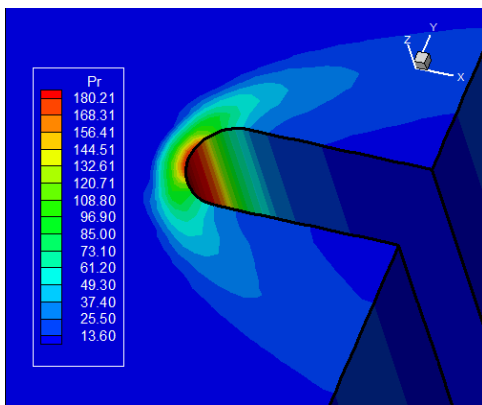


**Fig. 25. Pressure contours (ENO-NEWTON-5th-VL)**
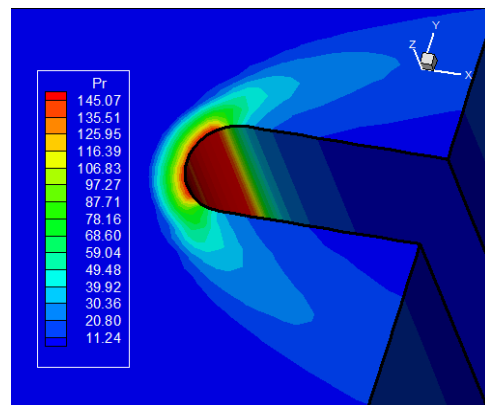


**Fig. 26. Pressure contours (ENO-NEWTON-5th-LS)**
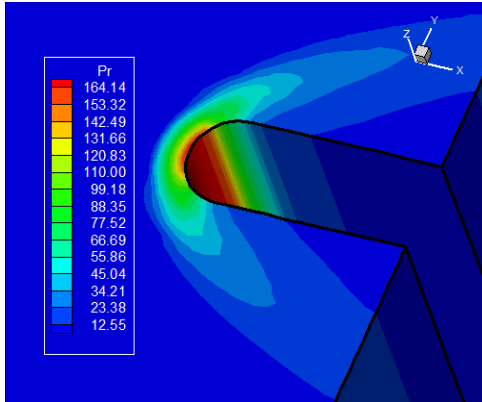
**Fig. 27. Pressure contours (ENO-HERMITE-3<sup>rd</sup>-VL)**
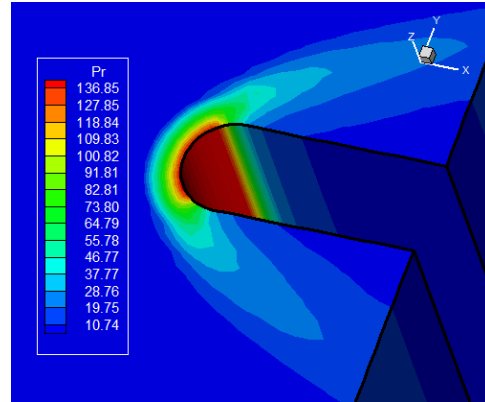


**Fig. 28. Pressure contours (ENO-HERMITE-3<sup>rd</sup>-LS)**
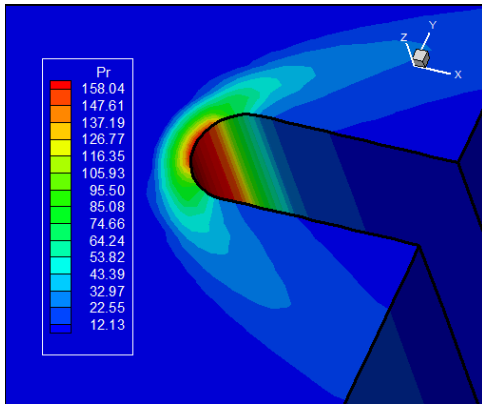


**Fig. 29. Pressure contours (ENO-HERMITE-5<sup>th</sup>-VL)**
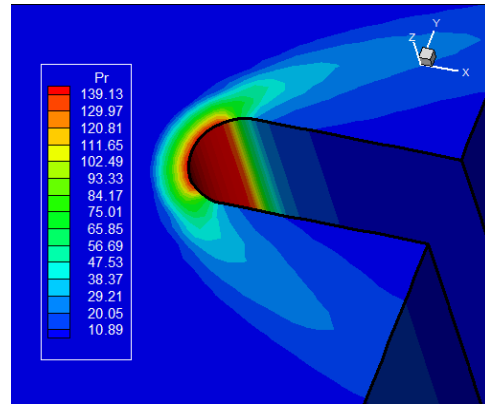


**Fig. 30. Pressure contours (ENO-HERMITE-5<sup>th</sup>-LS)**
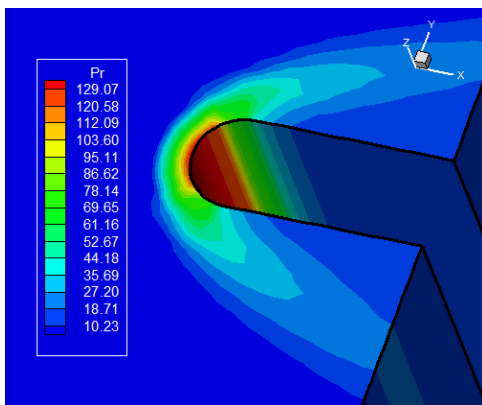


**Fig. 31. Pressure contours (WENO-NEWTON-3<sup>rd</sup>-VL)**
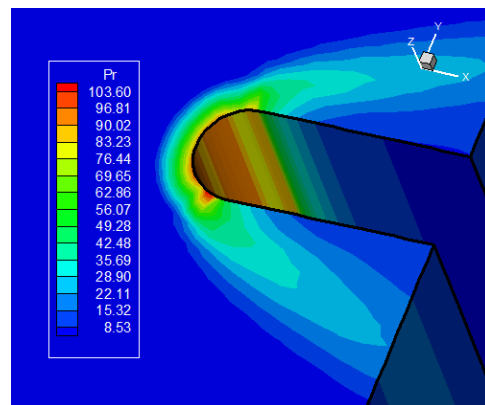


**Fig. 32. Pressure contours (WENO-NEWTON-3<sup>rd</sup>-LS)**

**VISCOUS CASE – FIVE SPECIES**
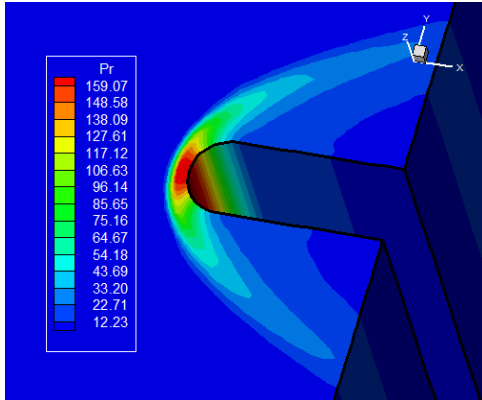


**Fig. 33. Pressure contours (MUSCL-2$^{nd}$-VL)**
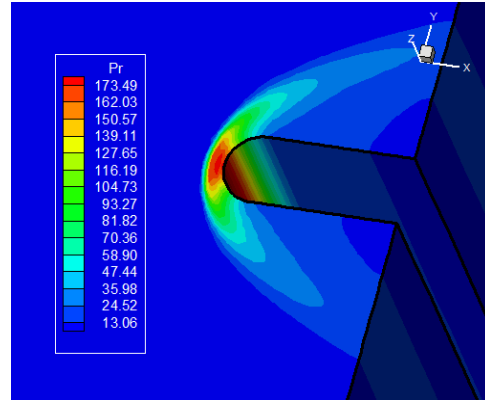


**Fig. 34. Pressure contours (ENO-NEWTON-3$^{rd}$-VL)**
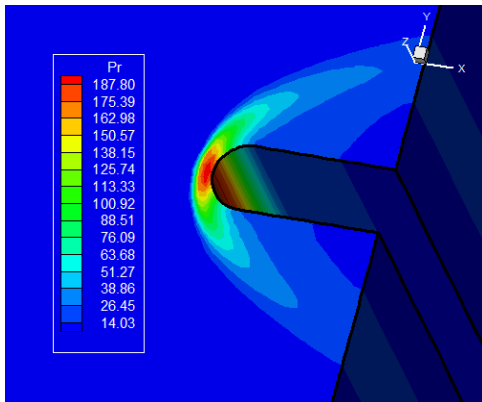


**Fig. 35. Pressure contours (ENO-NEWTON-4$^{th}$-VL)**
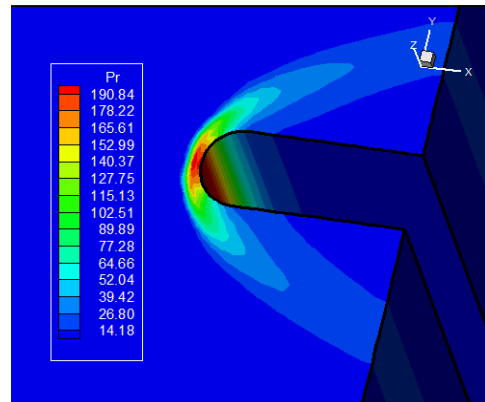


**Fig. 36. Pressure contours (ENO-NEWTON-4$^{th}$-LS)**

**VISCOUS CASE – SEVEN SPECIES**
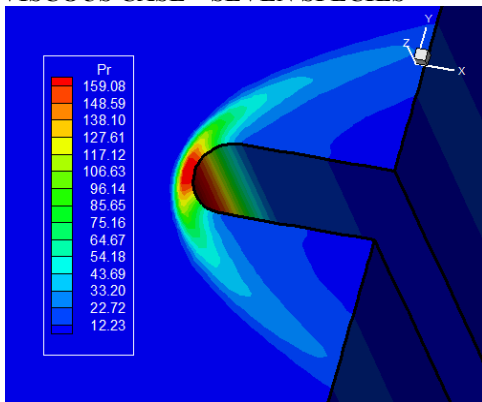


**Fig. 37. Pressure contours (MUSCL-2$^{nd}$-VL)**
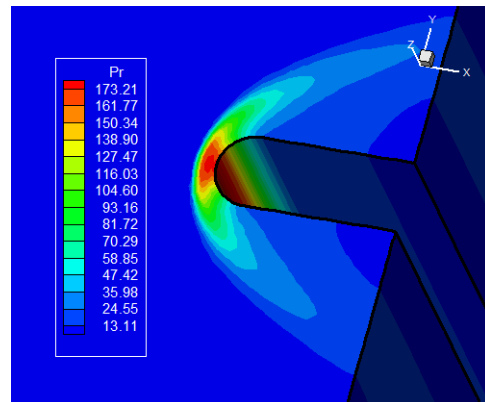


**Fig. 38. Pressure contours (ENO-NEWTON-3$^{rd}$-VL)**
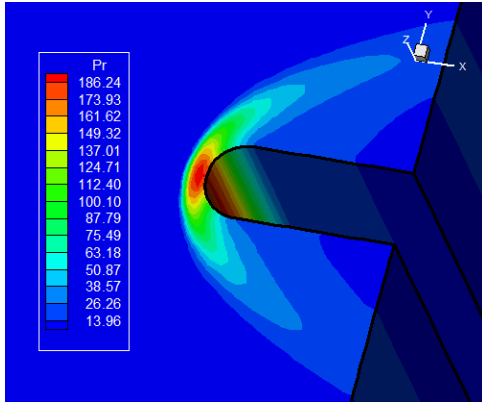
**Fig. 39. Pressure contours (ENO-NEWTON-4$^{th}$-VL)**
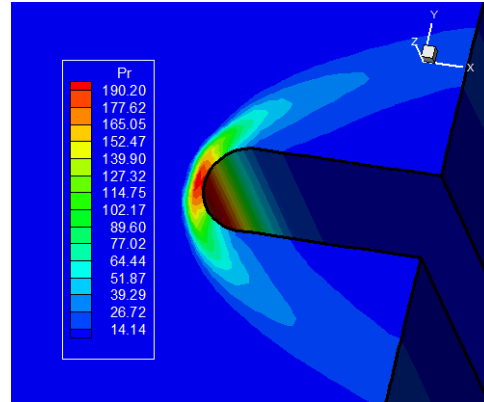


**Fig. 40. Pressure contours (ENO-NEWTON-4$^{th}$-LS)**

**Table 1. Values of r, c$_{rj}$ and $\overline{Q}$ (3$^{rd}$ Order)**

| r | c$_{r0}$ | $\overline{Q}$ | c$_{r1}$ | $\overline{Q}$ |
|---|---|---|---|---|
| 0 | ½ | $\overline{Q}_i$ | 1/2 | $\overline{Q}_{i+1}$ |
| 1 | -1/2 | $\overline{Q}_{i-1}$ | 3/2 | $\overline{Q}_i$ |

**Table 2. Values of r, $\overline{c}_{rj}$ and $\overline{Q}$ (3$^{rd}$ Order)**

| r | $\overline{c}_{r0}$ | $\overline{Q}$ | $\overline{c}_{r1}$ | $\overline{Q}$ |
|---|---|---|---|---|
| 0 | 3/2 | $\overline{Q}_i$ | -1/2 | $\overline{Q}_{i+1}$ |
| 1 | ½ | $\overline{Q}_{i-1}$ | 1/2 | $\overline{Q}_i$ |

**Table 3. Values of r, c$_{rj}$ and $\overline{Q}$ (5$^{th}$ Order)**

| r | c$_{r0}$ | $\overline{Q}$ | c$_{r1}$ | $\overline{Q}$ | c$_{r2}$ | $\overline{Q}$ |
|---|---|---|---|---|---|---|
| 0 | 1/3 | $\overline{Q}_i$ | 5/6 | $\overline{Q}_{i+1}$ | -1/6 | $\overline{Q}_{i+2}$ |
| 1 | -1/6 | $\overline{Q}_{i-1}$ | 5/6 | $\overline{Q}_i$ | 1/3 | $\overline{Q}_{i+1}$ |
| 2 | 1/3 | $\overline{Q}_{i-2}$ | -7/6 | $\overline{Q}_{i-1}$ | 11/6 | $\overline{Q}_i$ |

**Table 4. Values of r, $\overline{c}_{rj}$ and $\overline{Q}$ (5$^{th}$ Order)**

| r | $\overline{c}_{r0}$ | $\overline{Q}$ | $\overline{c}_{r1}$ | $\overline{Q}$ | $\overline{c}_{r2}$ | $\overline{Q}$ |
|---|---|---|---|---|---|---|
| 0 | 11/6 | $\overline{Q}_i$ | -7/6 | $\overline{Q}_{i+1}$ | 1/3 | $\overline{Q}_{i+2}$ |
| 1 | 1/3 | $\overline{Q}_{i-1}$ | 5/6 | $\overline{Q}_i$ | -1/6 | $\overline{Q}_{i+1}$ |
| 2 | -1/6 | $\overline{Q}_{i-2}$ | 5/6 | $\overline{Q}_{i-1}$ | 1/3 | $\overline{Q}_i$ |

**Table 5. Initial conditions to the problem of the blunt body**

| Property | Value |
|---|---|
| $M_\infty$ | 8.78 |
| $\theta$ (attack) | 0.0° |
| $\psi$ (longitudinal) | 0.0° |
| $\rho_\infty$ | 0.00326 kg/m$^3$ |
| $p_\infty$ | 687 Pa |
| $U_\infty$ | 4,776 m/s |
| $T_\infty$ | 694 K |
| Altitude | 40,000 m |
| $c_N$ | $10^{-9}$ |
| $c_O$ | 0.07955 |
| $c_{O2}$ | 0.13400 |
| $c_{NO}$ | 0.05090 |
| $c_{NO+}$ | 0.0 |
| $c_{e-}$ | 0.0 |
| L | 2.0 m |
| $Re_\infty$ | 2.389x10$^6$ |

**Table 6. Values of stagnation pressure and errors ([25] data)**

| Case | Procedure | $pr_0$ | Error (%) |
|---|---|---|---|
| | MUSCL – 2$^{nd}$ | 126.33 | 29.46 |
| | Newton – 2$^{nd}$ | 180.61 | 0.84 |
| | Newton – 3$^{rd}$ | - | - |
| Inviscid | Newton – 4$^{th}$ | 183.63 | 2.53 |
| TCNE[1] | Newton – 5$^{th}$ | 180.26 | 0.65 |
| | Hermite – 3$^{rd}$ | 164.25 | 8.29 |
| | Hermite – 5$^{th}$ | 158.13 | 11.71 |
| | WENO – 3$^{rd}$ | 129.06 | 27.94 |
| | WENO – 5$^{th}$ | - | - |
| | MUSCL – 2$^{nd}$ | 159.07 | 11.18 |
| | Newton – 2$^{nd}$ | - | - |
| | Newton – 3$^{rd}$ | 173.49 | 3.13 |
| Viscous | Newton – 4$^{th}$ | 187.80 | 4.86 |
| TCNE | Newton – 5$^{th}$ | - | - |
| | Hermite – 3$^{rd}$ | - | - |
| | Hermite – 5$^{th}$ | - | - |
| | WENO – 3$^{rd}$ | - | - |
| | WENO – 5$^{th}$ | - | - |

[1]*: Thermochemical Non-Equilibrium.*

**Table 7. Values of stagnation pressure and errors ([26] data)**

| Case | Procedure | $pr_0$ | Error (%) |
|---|---|---|---|
| | MUSCL – 2$^{nd}$ | 135.24 | 24.49 |
| | Newton – 2$^{nd}$ | 151.18 | 15.59 |
| | Newton – 3$^{rd}$ | 143.31 | 19.98 |
| Inviscid | Newton – 4$^{th}$ | 146.95 | 17.95 |
| TCNE | Newton – 5$^{th}$ | 146.14 | 18.40 |
| | Hermite – 3$^{rd}$ | 136.87 | 23.58 |
| | Hermite – 5$^{th}$ | 139.26 | 22.24 |
| | WENO – 3$^{rd}$ | 107.00 | 40.26 |

| Case | Procedure | $pr_0$ | Error (%) |
|------|-----------|--------|-----------|
| | WENO – $5^{th}$ | - | - |
| | MUSCL – $2^{nd}$ | - | - |
| | Newton – $2^{nd}$ | - | - |
| | Newton – $3^{rd}$ | - | - |
| Viscous | Newton – $4^{th}$ | 194.84 | 8.79 |
| TCNE | Newton – $5^{th}$ | - | - |
| | Hermite – $3^{rd}$ | - | - |
| | Hermite – $5^{th}$ | - | - |
| | WENO – $3^{rd}$ | - | - |
| | WENO – $5^{th}$ | - | - |

**Table 8. Values of stagnation pressure and errors ([25] data)**

| Case | Procedure | $pr_0$ | Error (%) |
|------|-----------|--------|-----------|
| | MUSCL – $2^{nd}$ | 126.29 | 29.49 |
| | Newton – $2^{nd}$ | 180.61 | 0.84 |
| | Newton – $3^{rd}$ | - | - |
| Inviscid | Newton – $4^{th}$ | 183.45 | 2.37 |
| TCNE | Newton – $5^{th}$ | 180.21 | 0.62 |
| | Hermite – $3^{rd}$ | 164.14 | 8.35 |
| | Hermite – $5^{th}$ | 158.04 | 11.76 |
| | WENO – $3^{rd}$ | 129.07 | 27.93 |
| | WENO – $5^{th}$ | - | - |
| | MUSCL – $2^{nd}$ | 159.08 | 11.18 |
| | Newton – $2^{nd}$ | - | - |
| | Newton – $3^{rd}$ | 173.21 | 3.29 |
| Viscous | Newton – $4^{th}$ | 186.24 | 3.99 |
| TCNE | Newton – $5^{th}$ | - | - |
| | Hermite – $3^{rd}$ | - | - |
| | Hermite – $5^{th}$ | - | - |
| | WENO – $3^{rd}$ | - | - |
| | WENO – $5^{th}$ | - | - |

**Table 9. Values of stagnation pressure and errors ([26] data)**

| Case | Procedure | $pr_0$ | Error (%) |
|------|-----------|--------|-----------|
| | MUSCL – $2^{nd}$ | 135.24 | 24.49 |
| | Newton – $2^{nd}$ | 151.18 | 15.59 |
| | Newton – $3^{rd}$ | - | - |
| Inviscid | Newton – $4^{th}$ | 146.09 | 18.43 |
| TCNE | Newton – $5^{th}$ | 145.07 | 19.00 |
| | Hermite – $3^{rd}$ | 136.85 | 23.59 |
| | Hermite – $5^{th}$ | 139.13 | 22.32 |
| | WENO – $3^{rd}$ | 103.60 | 42.16 |
| | WENO – $5^{th}$ | - | - |
| | MUSCL – $2^{nd}$ | - | - |
| | Newton – $2^{nd}$ | - | - |
| | Newton – $3^{rd}$ | - | - |
| Viscous | Newton – $4^{th}$ | 190.20 | 6.20 |
| TCNE | Newton – $5^{th}$ | - | - |
| | Hermite – $3^{rd}$ | - | - |
| | Hermite – $5^{th}$ | - | - |
| | WENO – $3^{rd}$ | - | - |
| | WENO – $5^{th}$ | - | - |

**Table 10. Computational data of the [25] scheme (5 Species)**

| Case | Procedure | CFL | Iterations |
|------|-----------|-----|------------|
| | MUSCL – $2^{nd}$ | 0.010 | 16,927 |
| | Newton – $2^{nd}$ | 0.010 | 37,224 |
| | Newton – $3^{rd}$ | - | - |
| Inviscid | Newton – $4^{th}$ | 0.010 | 27,768 |
| TCNE | Newton – $5^{th}$ | 0.010 | 19,841 |
| | Hermite – $3^{rd}$ | 0.010 | 17,637 |
| | Hermite – $5^{th}$ | 0.010 | 17,919 |
| | WENO – $3^{rd}$ | 0.010 | 18,048 |
| | WENO – $5^{th}$ | - | - |
| | MUSCL – $2^{nd}$ | 0.010 | 39,645 |
| | Newton – $2^{nd}$ | - | - |
| | Newton – $3^{rd}$ | 0.010 | 27,769 |
| Viscous | Newton – $4^{th}$ | 0.010 | 28,030 |
| TCNE | Newton – $5^{th}$ | - | - |
| | Hermite – $3^{rd}$ | - | - |
| | Hermite – $5^{th}$ | - | - |
| | WENO – $3^{rd}$ | - | - |
| | WENO – $5^{th}$ | - | - |

**Table 11. Computational data of the [26] scheme (5 Species)**

| Case | Procedure | CFL | Iterations |
|------|-----------|-----|------------|
| | MUSCL – $2^{nd}$ | 0.010 | 20,533 |
| | Newton – $2^{nd}$ | 0.010 | 37,709 |
| | Newton – $3^{rd}$ | 0.010 | 33,700 |
| Inviscid | Newton – $4^{th}$ | 0.010 | 39,792 |
| TCNE | Newton – $5^{th}$ | 0.010 | 44,477 |
| | Hermite – $3^{rd}$ | 0.010 | 30,144 |
| | Hermite – $5^{th}$ | 0.010 | 27,548 |
| | WENO – $3^{rd}$ | 0.010 | 47,159 |
| | WENO – $5^{th}$ | - | - |
| | MUSCL – $2^{nd}$ | - | - |
| | Newton – $2^{nd}$ | - | - |
| | Newton – $3^{rd}$ | - | - |
| Viscous | Newton – $4^{th}$ | 0.010 | 32,477 |
| TCNE | Newton – $5^{th}$ | - | - |
| | Hermite – $3^{rd}$ | - | - |
| | Hermite – $5^{th}$ | - | - |
| | WENO – $3^{rd}$ | - | - |
| | WENO – $5^{th}$ | - | - |

**Table 12. Computational data of the [25] scheme (7 Species)**

| Case | Procedure | CFL | Iterations |
|------|-----------|-----|------------|
| | MUSCL – $2^{nd}$ | 0.010 | 16,774 |
| | Newton – $2^{nd}$ | 0.010 | 35,565 |
| | Newton – $3^{rd}$ | - | - |
| Inviscid | Newton – $4^{th}$ | 0.010 | 27,450 |
| TCNE | Newton – $5^{th}$ | 0.010 | 19,713 |
| | Hermite – $3^{rd}$ | 0.010 | 17,511 |
| | Hermite – $5^{th}$ | 0.010 | 17,784 |

| Case | Procedure | CFL | Iterations |
|------|-----------|-----|------------|
|  | WENO – 3$^{rd}$ | 0.010 | 17,830 |
|  | WENO – 5$^{th}$ | - | - |
|  | MUSCL – 2$^{nd}$ | 0.010 | 39,513 |
|  | Newton – 2$^{nd}$ | - | - |
|  | Newton – 3$^{rd}$ | 0.010 | 27,482 |
| Viscous | Newton – 4$^{th}$ | 0.010 | 28,177 |
| TCNE | Newton – 5$^{th}$ | - | - |
|  | Hermite – 3$^{rd}$ | - | - |
|  | Hermite – 5$^{th}$ | - | - |
|  | WENO – 3$^{rd}$ | - | - |
|  | WENO – 5$^{th}$ | - | - |

**Table 13. Computational data of the [26] scheme (7 Species)**

| Case | Procedure | CFL | Iterations |
|------|-----------|-----|------------|
|  | MUSCL – 2$^{nd}$ | 0.010 | 20,287 |
|  | Newton – 2$^{nd}$ | 0.010 | 37,263 |
|  | Newton – 3$^{rd}$ | - | - |
| Inviscid | Newton – 4$^{th}$ | 0.010 | 39,278 |
| TCNE | Newton – 5$^{th}$ | 0.010 | 43,906 |
|  | Hermite – 3$^{rd}$ | 0.010 | 29,745 |
|  | Hermite – 5$^{th}$ | 0.010 | 27,177 |
|  | WENO – 3$^{rd}$ | 0.010 | 46,629 |
|  | WENO – 5$^{th}$ | - | - |
|  | MUSCL – 2$^{nd}$ | - | - |
|  | Newton – 2$^{nd}$ | - | - |
|  | Newton – 3$^{rd}$ | - | - |
| Viscous | Newton – 4$^{th}$ | 0.010 | 29,250 |
| TCNE | Newton – 5$^{th}$ | - | - |
|  | Hermite – 3$^{rd}$ | - | - |
|  | Hermite – 5$^{th}$ | - | - |
|  | WENO – 3$^{rd}$ | - | - |
|  | WENO – 5$^{th}$ | - | - |

# 11. Conclusions

The present work studied the reentry 3D-flows problem using high order resolution schemes, employing both Euler and Navier-Stokes equations under conservative and finite volume approaches. The ENO procedure was presented to a conserved variable interpolation process, using either the Newton method, to second-, third-, fourth- and fifth-orders of accuracy, or the Hermite method, to third- and fifth-orders of accuracy, and the WENO procedure is presented, using the Newton interpolation process, to generate third- and fifth-orders of accuracy solutions. The MUSCL scheme were also tested to serve as TVD benchmark solution. The "hot gas" hypersonic 3D-flow around a blunt body was carried out. The convergence process was accelerated to steady state condition through a spatially variable time step procedure, which has provided effective gains in terms of computational acceleration. The reactive simulations involved Earth atmosphere chemical models of five and seven species, based on the [29] and [30] models, respectively.

The results have indicated that the ENO procedure using Newton 5th-order interpolation process presents better solutions in both qualitative and quantitative features. The best ENO convergence was due to the [25] algorithm using Hermite interpolation in its 3rd-order of accuracy for both chemical models. The best global convergence was also due to the [25] algorithm using MUSCL procedure for both chemical models. It is important to note that considering the ENO procedure using the Newton interpolation, errors less than 3.00%

were found with the [25] numerical algorithm in the inviscid case and less than 4.00% for the viscous case. Moreover, using Hermite interpolation, errors inferior to 12.00% were found with the [25] numerical algorithm in the inviscid case.

This work can be considered an useful contribution to the CFD community in terms of considering the application of high order resolution methods to obtain thermochemical non-equilibrium 3D-flow solution. MUSCL, ENO and WENO procedures were implemented and tested in the solution of the "hot gas" blunt body problem. Suitable results were obtained with the ENO procedure in its 5th-order of accuracy, which is recommended for the present authors as the best technique to simulate reactive flow problems. Moreover, the code was validated with analysis of errors for the two algorithms under study, as suggested by Tables 6, 7, 8, 9. The authors intend that these comparisons are satisfactory to validate the code.

Other studies in the current literature did not perform comparisons involving MUSCL, ENO and WENO high order procedures altogether, which characterizes this work as original and innovative. It is possible to cite two examples: The work of [43] developed a numerical algorithm for solving the equations describing chemically reacting supersonic flows. The algorithm employed a two-stage Runge-Kutta method for integrating the equations in time and a Chebyshev spectral method for integrating the equations in space. The accuracy and efficiency of the technique was addressed by comparison with an existing implicit finite-difference procedure for modelling chemical reacting flows. This work was in two-dimensions; and the work of [44] developed a code capable to accurately modelling free-stream acoustic disturbances with non-equilibrium effects and to present preliminaries findings on the non-equilibrium effects on receptivity. They used a two-dimensional high-order shock-fitting finite-difference solver. As can be seen, although numerous works exist in the CFD literature about chemically reacting flows and high order resolution, the main features of the present work, which enhances high resolution through the use of three different procedures, on a context of thermochemical non-equilibrium, and using two different upwind numerical algorithms in finite volumes and three-dimensions, are representative of the originality and innovation of the present article.

The impact of this article is to give to other authors the necessary tools to perform high order numerical simulations of fluid flow under re-entry conditions. Countries like Turkey are developing their own aerospace program, and articles like this, presenting high order resolution of re-entry flow experiments, are vital and important to their development. For future works, the intention is to extend this research to perform high order resolution using spectral methods for flows under reactive + turbulent + magnetic field conditions, resulting in more realistic simulations and state of art research.

Finally, the developed code is an in-house version and was written in FORTRAN90 by the first author. The authors did not use commercial computer code for this study.

## Acknowledgements

## Competing Interests

Authors have declared that no competing interests exist.

## References

[1]     Gupta RN, Yos JM, Thompson RA, Lee KP. A review of reaction rates and thermodynamic and transport properties for an 11-Species Air Model for Chemical and Thermal Nonequilibrium Calculations to 30000 K", NASA RP-1232; 1990.

[2]     Park C. Radiation enhancement by nonequilibrium in earth's atmosphere. Journal of Spacecraft and Rockets. 1985;22(1):27-36.

[3]     Park C. Problem of rate chemistry in the flight regimes of aeroassissted orbital transfer vehicles, thermal design of aeroassissted orbital transfer vehicles, Progress in Astronautics and Aeronautics, edited by H. F. Nelson, AIAA, NY. 1985;96:511-537.

[4]     Gnoffo PA. Three-dimensional AOTV Flowfields in Chemical Nonequilibrium. AIAA Paper 86-0230; 1986.

[5]     Li CP. Implicit methods for computing chemically reacting flow. NASA TM-58274; 1986.

[6]     Lee JH. Basic governing equations for the flight regimes of aeroassisted orbital transfer vehicles. Thermal Design of Aeroassisted Transfer Vehicles, Progress in Astronautics and Aeronautics, AIAA. 1985;96:3-53.

[7]     Park C. Convergence of computation of chemically reacting flows. Thermophysical Aspects of Re-entry Flows, Progress in Astronautics and Aeronautics, edited by J. N. Moss and C. D. Scott, AIAA, NY. 103:478-513.

[8]     Park C. Assessment of two-temperature kinetic model for dissociating and weakly-ionizing nitrogen. AIAA Paper 86-1347; 1986.

[9]     Park C. Calculation of nonequilibrium radiation in the flight regimes of aeroassissted orbital transfer vehicles. Thermal Design of Aeroassissted Orbital Transfer Vehicles, Progress in Astronautics and Aeronautics, edited by H. F. Nelson, AIAA, NY. 1985;96:395-418.

[10]    Park C. Nonequilibrium air radiation (NEQAIR) program: User's manual. NASA TM-86707; 1985.

[11]    Van Der Vegt JJ. ENO-Osher schemes for Euler equations. AIAA Paper 93-0335; 1993.

[12]    Goodman J, LeVeque R. On the accuracy of stable schemes for 2D scalar conservation laws. Mathematics of Computation. 1985;45:15-21.

[13]    Osher S, Chakravarthy SR. High resolution schemes and the entropy condition. SIAM Journal on Numerical Analysis. 1984;21:955-984.

[14]    Hirsch C. Numerical computation of internal and external flows computational methods for inviscid and viscous flows. John Wiley & Sons Ltd. 1990;691.

[15]    Harten A, Osher S, Engquist B, Chakravarthy SR. Some results on uniformly high order accurate essentially non-oscillatory schemes. Journal of Applied Numerical Mathematics. 1986;2:347-377.

[16]    Harten A, Osher S. Uniformly high-order accurate nonoscillatory schemes I. SIAM Journal on Numerical Analysis. 1987;24:279-309.

[17]    Harten A, Engquist B, Osher S, Chakravarthy SR. Uniformly high order accurate essentially non-oscillatory schemes III. Journal of Computational Physics. 1987;71:231-303.

[18]    Harten A, Chakravarthy SR. Multi-dimensional ENO schemes for general geometries. ICASE Report 91-76, NASA Langley, Virginia; 1991.

[19]    Shu CW, Osher S. Efficient implementation of essentially non-oscillatory shock-capturing schemes. Journal of Computational Physics. 1988;77:439-471.

[20]   Shu CW, Osher S. Efficient implementation of essentially non-oscillatory shock capturing schemes, II. Journal of Computational Physics. 1989;83:32-78.

[21]   Atkinson KE. An introduction to numerical analysis. John Wiley & Sons, 2nd Edition. 1989;693.

[22]   Faires JD, Burden R. Numerical methods. Thomsom Books/Cole, 3rd Edition. 2003;622.

[23]   Liu XD, Osher S, Chan T. Weighted essentially non-oscillatory schemes. Journal of Computational Physics. 1994;115:200-212.

[24]   Shu CW. Essentially non-oscillatory and weighted essentially non-oscillatory schemes for hyperbolic conservation laws. ICASE Report No. 97-65; 1997.

[25]   Van Leer B. Flux-vector splitting for the Euler equations. Lecture Notes in Physics, Springer Verlag, Berlin. 1982;170:507-512.

[26]   Liou M, Steffen Jr., CJ. A new flux splitting scheme. Journal of Computational Physics. 1993;107: 23-39.

[27]   Maciel ESG. Simulations in 2D and 3D applying unstructured algorithms, Euler and Navier-Stokes Equations – Perfect Gas Formulation, Saarbrücken, Deutschland: Lambert Academic Publishing (LAP). 2015;Ch. 1:26-47.

[28]   Maciel ESG. Simulations in 2D and 3D applying unstructured algorithms, Euler and Navier-Stokes Equations – Perfect Gas Formulation, Saarbrücken, Deutschland: Lambert Academic Publishing (LAP). 2015;Ch. 6:160-181.

[29]   Saxena SK, Nair MT. An improved roe scheme for real gas flow. AIAA Paper 2005-587; 2005.

[30]   Blottner FG. Viscous shock layer at the stagnation point with nonequilibrium air chemistry. AIAA Journal. 1969;7(12):2281-2288.

[31]   Prabhu RK. An implementation of a chemical and thermal nonequilibrium flow solver on unstructured meshes and application to blunt bodies. NASA CR-194967; 1994.

[32]   Maciel ESG, Pimenta AP. Reentry flows in chemical non-equilibrium in two-dimensions. Proceedings of the 10th International Symposium on Combustion and Energy Utilization (ICCEU 2010), Mugla, Turkey; 2010.

[33]   Maciel ESG, Pimenta AP. Hypersonic reactive flow simulations in two- and three-dimensions, chemical and thermochemical non-equilibrium conditions, Saarbrücken, Deutschland: Lambert Academic Publishing (LAP). 2015;Ch. 5:274-330.

[34]   Maciel ESG. Applications of TVD algorithms in 2D and 3D, Euler and Navier-Stokes Equations in 2D and 3D, Saarbrücken, Deutschland: Lambert Academic Publishing (LAP). 2015;Ch. 13:463-466.

[35]   Van Leer B. Towards the ultimate conservative difference scheme. II. Monotonicity and Conservation Combined in a Second-Order Scheme", Journal of Computational Physics. 1974;14:361-370.

[36]   Roe PL. In proceedings of the AMS-SIAM "Summer Seminar on Large-Scale Computation in Fluid Mechanics", Edited by B. E. Engquist et al, Lectures in Applied Mathematics. 1983;22:163.

[37]   Ait-Ali-Yahia D, Habashi WG. Finite element adaptive method for hypersonic thermochemical nonequilibrium flows. AIAA Journal. 1997;35(8):1294-1302.

[38] Radespiel R, Kroll N. Accurate flux vector splitting for shocks and shear layers. Journal of Computational Physics. 1995;121:66-78.

[39] Long LN, Khan MMS, Sharp HT. Massively parallel three-dimensional Euler / Navier-Stokes Method. AIAA Journal. 1991;29(5):657-666.

[40] Fox RW, McDonald AT. Introdução à Mecânica dos Fluidos, Guanabara Editor; 1988.

[41] Maciel ESG. Comparison between Newton and Hermite ENO interpolations as applied to reentry flows in 2D. Computational and Applied Mathematics Journal. 2015;1(5):261-281.

[42] Anderson Jr., JD. Fundamentals of aerodynamics. McGraw-Hill, Inc., 5th Edition. 2010;1008.

[43] Drummond JP, Hussaini MY, Zang TA. Spectral method for modeling supersonic chemically reacting flowfields. AIAA Journal. 1986;24(9):1461-1467.

[44] Parsons N, Zhongy X, Kimz J, Eldredgex J. Numerical study of hypersonic receptivity with thermochemical non-equilibrium on a blunt cone. AIAA Paper 2010-4446; 2010.

_____